

1 This manuscript has been submitted for publication in Agricultural and Forest Meteorology. Please
2 note that, the manuscript is currently under review and has yet to be formally accepted for
3 publication. Subsequent versions of this manuscript may have slightly different content. If accepted,
4 the final version of this manuscript will be available via the 'Peer-reviewed Publication DOI' link

5
6 **STEEP: a remotely-sensed energy balance model for evapotranspiration estimation in**
7 **seasonally dry tropical forests**

8 Ulisses A. Bezerra^{a*}, John Cunha^a, Fernanda Valente^b, Rodolfo L. B. Nóbrega^c, João M. Andrade^d, Magna S.
9 B. Moura^e, Anne Verhoeff, Aldrin M. Perez-Marin^g, Carlos O. Galvão^a

10 ^aFederal University of Campina Grande, Centre for Natural Resources and Technology, Campina Grande, Brazil

11 ^bForest Research Centre (CEF), School of Agriculture, University of Lisbon, Tapada da Ajuda, 1349-017 Lisbon, Portugal

12 ^cImperial College London, Georgina Mace Centre for the Living Planet, Department of Life Sciences, Silwood Park
13 Campus, Buckhurst Road, Ascot, SL5 7PY, UK

14 ^dFederal University of Pernambuco, Department of Civil and Environmental Engineering, Recife, Brazil

15 ^eEmpresa Brasileira de Pesquisa Agropecuária, Embrapa Semiárido, Petrolina 56302-970, Brazil

16 ^fDepartment of Geography and Environmental Science, The University of Reading, United Kingdom

17 ^gInstituto Nacional do Semiárido/Núcleo de Desertificação e Agroecologia

18 *Corresponding author: ulisses.alencar@estudante.ufcg.edu.br

19
20 **Abstract**

21 Improvement of evapotranspiration (ET) estimates using remote sensing (RS) products based on
22 multispectral and thermal sensors has been a breakthrough in hydrological research. In large-scale
23 applications, methods that use the approach of RS-based surface energy balance (SEB) models
24 often rely on oversimplifications of the aerodynamic resistances. The use of these SEB models for
25 Seasonally Dry Tropical Forests (SDTF) has been challenging due to incompatibilities between the
26 assumptions underlying those models and the specificities of this environment, such as the highly
27 contrasting phenological phases or ET is mainly controlled by soil–water availability. We developed
28 a RS-based SEB model from a one-source bulk transfer equation, called STEEP. Our model uses
29 the Plant Area Index to represent the woody structure of the plants in calculating the moment
30 roughness length. In the aerodynamic resistance for heat transfer, the parameter kB^{-1} was included,
31 correcting it with RS soil moisture. Besides, the remaining λET in endmembers pixels was quantified

32 using the Priestley-Taylor equation. We implemented the STEEP algorithm on the Google Earth
33 Engine platform, using worldwide free data. Four sites with eddy covariance data located in the
34 Caatinga, the largest SDTF in South America, in the Brazilian semiarid region, were used to evaluate
35 the STEEP model. Our results show that STEEP based on the specific characteristics of the SDTF
36 increased the accuracy of ET estimates without requiring any additional climatological information.
37 This improvement is more pronounced during the dry season, which in general, ET for these SDTF
38 is overestimated by traditional SEB models, as happened in our research with the SEBAL. The
39 STEEP model had similar or superior behaviour and performance statistics relative to global ET
40 products (MOD16 and PMLv2). This work contributes to an improved understanding of the drivers
41 and modulators of the energy and water balances at local and regional scales in SDTF.
42 Keywords: Sensible heat flux, Aerodynamic resistance for heat transfer, Surface energy balance,
43 Caatinga, Google earth engine

44

45 1. Introduction

46 Quantifying evapotranspiration (ET) is one of the largest research challenges in hydrology
47 because ET is driven by a complex combination of atmospheric, vegetation, edaphic and terrain
48 characteristics (Wang et al., 2016; Bhattarai et al., 2017). The traditional techniques to quantify ET,
49 e.g. Bowen ratio or eddy covariance system (EC), are limited to areas up to ~ 1 km² (Allen et al.,
50 2011; Anapalli et al., 2016; Mcshane et al., 2017). Over the past decades, models based on satellite
51 remote sensing (RS) data have been increasingly developed and applied to estimate ET for multiple
52 temporal and spatial scales (Anderson et al., 2011; Chen and Liu, 2020). RS-based surface energy
53 balance (SEB) models estimate ET in terms of energy per unit area (W/m²), i.e. by latent heat flux,
54 λET , where λ is the latent heat of vaporization of water (Shuttleworth, 2012; Barraza et al., 2017).
55 SEB models obtain λET by subtracting the soil heat (G) and sensible heat (H) fluxes from the net
56 radiation (R_n). Estimates of R_n obtained with RS data have been improving, and this flux can
57 nowadays be estimated with acceptable precision (Allen et al., 2011; Ferreira et al., 2020). The $G:R_n$
58 ratio can be predicted with reasonable accuracy through the use of empirical relationships with soil,
59 vegetation, and temperature characteristics (Bastiaanssen, 1995; Murray and Verhoef, 2007; Allen
60 et al., 2011; Danelichen et al., 2014). Challenges in estimating λET as a residual of the energy

61 balance are mostly associated with the uncertainties in H (Gokmen et al., 2012; Paul et al., 2014;
62 Mohan et al., 2020a, b; Costa-Filho et al., 2021). The bulk heat transfer calculation that is used to
63 compute H involves variables related to the temperature gradient and to the aerodynamic resistance
64 for heat transfer (rah). If any of these variables are poorly estimated, the performance of SEB models
65 will be reduced (Verhoef et al., 1997a, b; Su et al., 2001; Gokmen et al., 2012; Costa-Filho et al.,
66 2021; Liu et al., 2021).

67 The difference between the aerodynamic surface temperature and air temperature (dT)
68 drives H . However, the lack of techniques to measure the aerodynamic surface temperature required
69 strategies to use the radiometric land surface temperature (LST) as an alternative. Bastiaanssen et
70 al. (1998), when creating the Surface Energy Balance Algorithms for Land (SEBAL), proposed that
71 dT can be estimated with a linear relationship on LST. This requires identifying areas with contrasting
72 extreme conditions in terms of cover and humidity, e.g., dry bare and well-watered soil surfaces,
73 commonly known as hot/dry and cold/wet endmembers, respectively. The sensible heat transfer
74 equation, in conjunction with the surface energy balance in hot/dry and cold/wet endmembers, allows
75 one to obtain the coefficients of the linear relationship between dT and LST. Bastiaanssen et al.
76 (1998) proposed the selection of endmembers by assuming that H in the cold/wet endmember and
77 the λET in the hot/dry endmember are zero. However, these assumptions are not necessarily valid
78 (Singh and Irmak, 2011; Singh et al., 2012). The cold/wet endmember refers to an area with a well-
79 irrigated crop surface having ground fully covered by vegetation, so it can be assumed that a non-
80 negligible amount of sensible heat can still be generated by such a surface. Similarly, for the hot/dry
81 endmember, an area dominated by bare soil, there may be a remaining λET resulting from
82 antecedent rainfall events. Some studies have quantified H and λET in hot/dry and cold/wet
83 endmembers (Trezza, 2006; Allen et al., 2007; Singh and Irmak, 2011); they have shown that this
84 quantification produces a better approximation of daily ET.

85 Based on the Monin-Obukhov similarity theory, rah is defined as a function of the momentum
86 ($z0m$) and heat ($z0h$) roughness lengths. Theoretically, the sum of the zero plane displacement
87 height ($d0$) together with $z0h$ defines the level of the effective source of sensible heat (Thom, 1972;
88 Chehbouni et al., 1996; Gokmen et al., 2012) and, therefore, $z0h$ constitutes one of the most crucial
89 parameters for the accurate calculation of H (Verhoef et al., 1997a; Su et al., 2001). However, as

90 $z0h$ cannot be measured directly, it is commonly calculated via the dimensionless parameter kB^{-1}
91 formulated to express the excess resistance of heat transfer compared to momentum transfer (Owen
92 and Thomson, 1963). In RS-based SEB models, oversimplifications are present in the calculation of
93 rah , e.g. different land use types are represented by the same values for $z0h$ (Bastiaanssen et al.,
94 2005; Allen et al., 2007) kB^{-1} (Bastiaanssen et al., 1998), or the values for the aerodynamic
95 parameters are kept constant in time and space. However, these parameters should not be
96 considered constant, nor set to zero, as this can lead to large inaccuracies in the estimates of H
97 (Verhoef et al., 1997a) and, consequently, of λET (Liu et al., 2007; Paul et al., 2014; Liu et al., 2021).
98 Studies have shown that kB^{-1} typically ranges from 1 to 12, depending on the dominant surface
99 coverage (Kustas et al., 1989; Troufleau et al., 1997; Verhoef et al., 1997a; Lhomme et al., 2000; Su
100 et al., 2001). Studies illustrate that if an appropriate value of kB^{-1} is used, H can be accurately
101 estimated using LST via the bulk transfer method (Stewart et al., 1994; Su et al., 2001; Jia et al.,
102 2003; Paul et al., 2013).

103 Another problem with RS-based SEB models is that these methods are imprecise when
104 applied to non-agricultural environments, such as forests, deserts, sparse savannahs or rangelands
105 and riparian systems, because of the heterogeneous nature of the vegetation, terrain, soils, and
106 water availability in these environments. This causes the flux estimates obtained with the SEB
107 method, and the underlying aerodynamic parameters, to be highly variable (Allen et al., 2011;
108 Gokmen et al., 2012; Barraza et al., 2017; Chen and Liu, 2020; Costa-Filho et al., 2021). This is
109 especially true in Seasonally Dry Tropical Forests (SDTF) regions, where there is a large spatio-
110 temporal variation in vegetation density, in vegetation structural parameters such as canopy height,
111 crown shape and branching, and water availability. SDTF are an important tropical biome and one
112 of the most threatened ecoregions of the world (Moro et al., 2015; Pennington et al., 2018). SDTF
113 are broadly defined as forest formations in tropical regions characterised by marked seasonality in
114 rainfall distribution, resulting in a prolonged dry season that usually lasts five or six months
115 (Pennington et al., 2009; Paloschi et al., 2020). The most extensive contiguous areas of SDTF are
116 in the neotropics, comprising more than 60% of the remaining global stands of this vegetation (Miles
117 et al., 2006; Queiroz et al., 2017). The physiognomies exhibited by SDTF are heterogeneous, with
118 vegetation ranging from tall forests with closed canopies to scrublands rich in succulents and thorn-

119 bearing plants (Moro et al., 2015; Paloschi et al., 2020). SDTF foliage patterns are adapted to the
120 intense climate and water seasonality, which is highly dependent on interannual climate variability
121 (Alberton et al., 2017; Medeiros et al., 2022). The vegetation drops most leaves during the dry
122 season, and the first rainfall events trigger a rapid leaf growth in the wet season (Alberton et al.,
123 2017; Paloschi et al., 2020; Medeiros et al., 2022). SDTF are being rapidly degraded (12% between
124 1980 and 2000), highlighting an urgent priority for their conservation (Moro et al., 2015; Maia et al.,
125 2020). The risks faced by SDTF mainly stem from anthropogenic disturbance effects, which range
126 from local habitat loss to global climate change, leading to biodiversity loss and reductions in biomass
127 (Allen et al., 2017; Maia et al., 2020).

128 Application of SEB models to estimate evapotranspiration over SDTF has been challenging
129 due to the incompatibility between the existing assumptions of the models and the specificities of
130 these forests. Precipitation seasonality is the primary phenological regulator of SDTF (Moro et al.,
131 2016; Campos et al., 2019; Paloschi et al., 2020), and land-cover patterns show distinct intra- and
132 inter-annual spectral responses (Cunha et al., 2020; Andrade et al., 2021; Medeiros et al., 2022).
133 Therefore, biophysical remotely-sensed variables, such as Normalized Difference Vegetation Index
134 (NDVI) and surface albedo, which are usually used to select the endmembers, exhibit high spatial
135 and temporal variability in SDTF, which causes ET estimates from the SEB models to lack fidelity
136 (Silva et al., 2019). Selection of suitable roughness parameters such as z_{0m} , d_0 , and kB^{-1} is
137 important for the correct quantification of the energy balance in SDTF. However, these parameters
138 are more challenging to obtain in SDTF than for evergreen forests, as in addition to vegetation height,
139 other characteristics such as plant density, above-ground plant structure and the strong seasonality
140 of phenology (Alberton et al., 2017; Miranda et al., 2020; Paloschi et al., 2020) have a considerable
141 effect on the turbulent transfer in these forests. Another key issue is how to verify the results of SEB
142 methods due to the scarcity, in many regions, of terrestrial observations and the uneven
143 spatiotemporal distribution of monitoring data. SEB models may not satisfactorily represent ET in
144 regions with sparse vegetation and high climatic seasonality, such as SDTF (Senkondo et al., 2019;
145 Laipelt et al., 2021; Melo et al., 2021). The main reason is that these methods have generally been
146 evaluated and/or parameterized using sites located in other ecosystems and climates in North
147 America, Europe, Australia, East Asia, and in agricultural regions that have characteristics quite

148 distinct from SDTF (Melo et al., 2021). Therefore, a better quantification of ET, especially in regions
149 with high climatic seasonality, will help to design better water management policies that will be able
150 to deal with the effects of climate variability, land use/cover and climate changes (Lima et al., 2021).

151 We hypothesise that a SEB model that improves or considers estimates of $z0m$, kB^{-1} , and
152 therefore of rah for the SDTF will improve H and ET estimates of these forests. To test this
153 assumption, we introduce a novel SEB model based upon a one-source bulk transfer equation,
154 herein referred to as Seasonal Tropical Ecosystem Energy Partitioning (STEEP). The STEEP model
155 aims to improve H and ET estimates for SDTF by incorporating the woody structure of plants through
156 the Plant Area Index (PAI), and soil moisture obtained by remote sensing to help represent the
157 seasonality of the aerodynamic and surface variables that drive the energy fluxes. In addition, our
158 approach when calculating dT uses the concept of the linear relationship in LST. To obtain its
159 coefficients, we compute, in the hot/dry and cold/wet endmembers, H by the surface energy balance,
160 and the remaining λET through the principle of the Priestley-Taylor equation. STEEP is designed to
161 take advantage of the extensive free database available on the Google Earth Engine (GEE) cloud
162 computing environment. STEEP is herein evaluated at the field scale against four flux towers in the
163 Caatinga, the largest continuous SDTF in the Americas. Additionally, the model was compared with
164 SEBAL and two consolidated global ET products: MOD16 (Mu et al., 2011; Running et al., 2017)
165 and PMLv2 (Zhang et al., 2019).

166

167 **2. Methodology**

168 2.1 Study areas and respective data

169 The study concerns the Brazilian Caatinga, the largest continuous SDTF in the Americas,
170 located between the Equator and the Tropic of Capricorn (about 3° and 18° south), in the Brazilian
171 semiarid region. It covers an area of about 850,000 km² (Silva et al., 2017a; Andrade et al., 2021;
172 Brazil MMA, 2021). The climate in the Caatinga is characterized by high air temperatures (around
173 26° to 30° C) and high potential evapotranspiration (1,500 to 2,000 mm/year) coupled with low annual
174 rainfall (300 to 800 mm/year, normally concentrated in 3–6 months) with high intra- and inter-annual
175 variability in space and time, and a long dry season which sometimes lasts up to 11 months in some
176 areas of Caatinga (Moro et al., 2016; Miranda et al., 2018; Paloschi et al., 2020). The Caatinga

177 vegetation has at least thirteen physiognomies ranging from woods to sparse thorny shrubs,
178 morphologically adapted to resist water stress and high air temperatures (Araújo et al., 2009; Silva
179 et al., 2017a; Marques et al., 2020; Miranda et al., 2020), and it has been identified as one of the
180 most biodiverse SDTF regions globally (Pennington et al., 2006; Santos et al., 2014; Koch et al.,
181 2017). Still, the Caatinga and other SDTF are among the least studied ecoregions compared to
182 tropical forests and savannas (Santos et al., 2012; Koch et al., 2017; Tomasella et al., 2018; Borges
183 et al., 2020). Only 1% of the Brazilian Caatinga area is legally protected (Koch et al., 2017).

184 We used data from four sites located in the Caatinga (Fig. 1 and Table 1). Located on
185 crystalline terrain (Fig. 1a), these Caatinga sites have soils with highly variable properties, ranging
186 from fertile (those with a clayey texture) to poor (those soils that are sandier). However, most soils
187 of the SDTF are typically shallow and stony (i.e. Entisols, Alfisols, and Ultisols; WRB, 2006), retaining
188 water only for a short period between rainfall events and after the rainy season (Moro et al., 2015;
189 Queiroz et al., 2017). The climate of the four observation sites is semi-arid, type BSh (Fig. 1b)
190 according to the Köppen climate classification (Alvares et al., 2013).

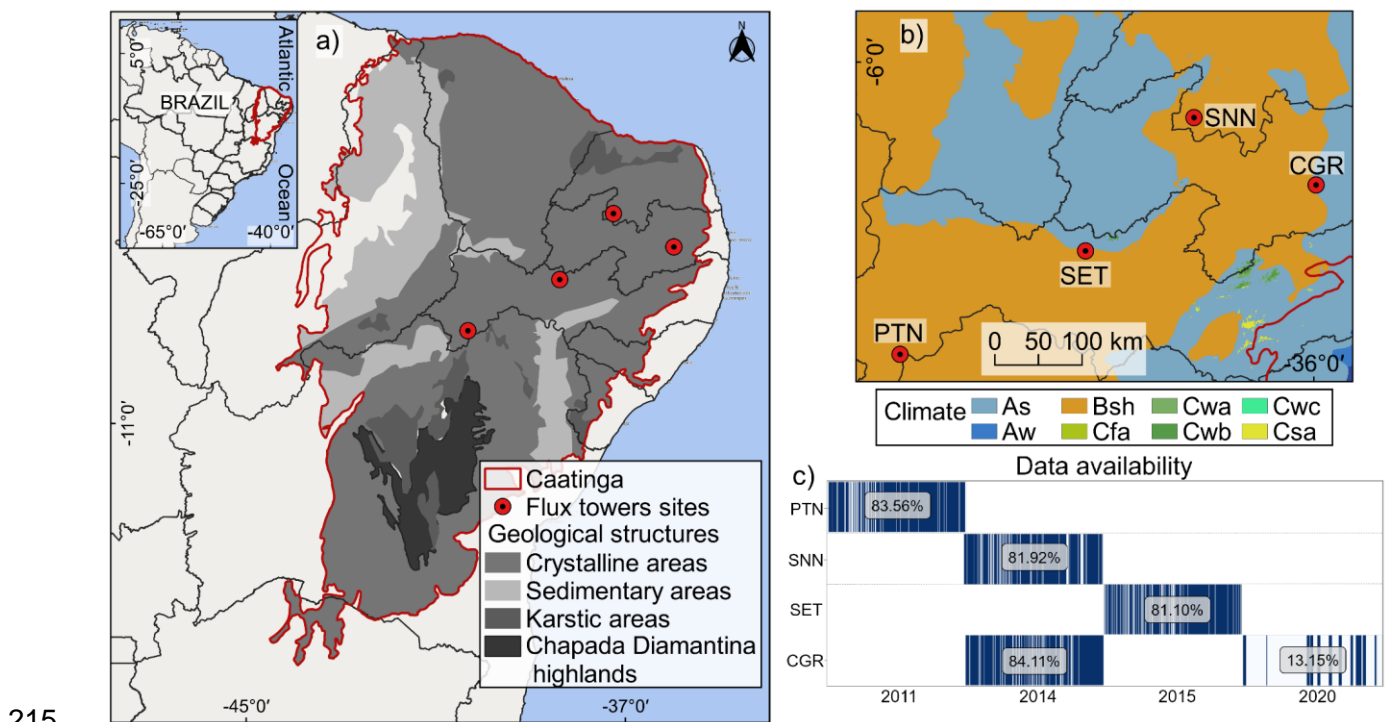
191 Eddy covariance data, covering several periods from 2011 to 2020 (Fig. 1c), were used to
192 evaluate the modelled ET and H . The four sites were instrumented with flux towers equipped with
193 three-dimensional ultrasonic anemometers (CSAT3, Campbell Scientific Inc., Logan, UT, USA) and
194 open-path infrared gas analyzers (LI-7500, LI-COR Inc., Lincoln, NE, USA, in the PTN site, or
195 EC150, Campbell Scientific Inc., Logan, UT, USA, in the other three sites). ET data for the PTN,
196 SNN and SET sites have been previously described; they underwent standard procedures to ensure
197 their quality and were published by Melo et al. (2021). Observations at the CGR site were collected
198 through two micrometeorological towers, located in a dense Caatinga area within the Brazilian
199 National Institute of Semiarid (INSA) experimental area, a 300 ha forest reserve with different stages
200 of regeneration. The first tower (height of 7 m) was active between the years of 2014 and 2017, as
201 described in Oliveira et al. (2021). The second tower (height of 15 m) is part of the Caatinga
202 Observatory (OCA) and includes an EC system that has been collecting data since 2020. The OCA
203 is a laboratory maintained by the Federal University of Campina Grande and INSA. H data for the
204 PTN, SNN and CGR sites have been obtained from the respective principal investigators, while data
205 for the SET site have been obtained from the AmeriFlux network (Antonino, 2019). For the retrieval

206 of λET and H , we used the LoggerNet software (Campbell Scientific, Inc., Logan, UT, USA) in order
 207 to transform 10 Hz raw data into 30 min binaries. Afterwards, EdiRe software was used to process
 208 the high-frequency data, averaging every 30 min. Detailed information on data processing, quality
 209 control, and post-processing can be found in Campos et al. (2019) and Cabral et al. (2020). In
 210 addition, data for any day with rain greater than 0.5 mm was removed. The daily ET was calculated
 211 using the daily average λET .

212 Table 1. List of EC-equipped flux tower observation sites in the study area.

Sites	State of Brazil	Mean annual of rainfall (mm) ¹	Site average elevation (m)	Location (Lon;Lat)	Data availability	Main reference
Petrolina (PTN)	Pernambuco	428.6	395	-40.3212; -9.0465	Jan–Dec 2011	Souza et al. (2015)
Serra Negra do Norte (SNN)	Rio Grande do Norte	629.5	205	-37.2514; -6.5783	Jan–Dec 2014	Marques et al. (2020)
Serra Talhada (SET)	Pernambuco	648	465	-38.3842; -7.9682	Jan–Dec 2015	Silva et al. (2017b)
Campina Grande (CGR)	Paraíba	777	490	-35.9763; -7.2805	Jan–Dec 2014	Oliveira et al. (2021)
Campina Grande (CGR)	Paraíba	777	490	-35.9763; -7.2805	Jan–Dec 2020	This study

213 ¹ Rainfall Data Sources: Brazilian National Institute of Meteorology (INMET) and Pernambuco State
 214 Agency for Water and Climate (APAC).



216 Figure 1. Location of flux tower observation sites in Caatinga. a) Geographical overview of the
217 Caatinga (Moro et al., 2015), b) Köppen's climate classification map according to Alvares et al.
218 (2013) and c) Data availability on the observation sites.

219 2.2 The Seasonal Tropical Ecosystem Energy Partitioning (STEEP) model

220 SEB models have been applied in many parts of the world (Mohan et al., 2020a). The one-
221 source SEB models that are most commonly found in the literature are SEBAL (Bastiaanssen et al.,
222 1998), Surface Energy Balance System (SEBS; Su, 2002), Mapping EvapoTranspiration at high
223 Resolution with Internal Calibration (METRIC; Allen et al., 2007), and Operational Simplified Surface
224 Energy Balance (SSEBop; Senay et al., 2013). As in other SEB models, STEEP performs the energy
225 balance at the time of satellite overpass (instantaneous) to obtain λET as the surface energy balance
226 residual. The computation of R_n and G , necessary to get λET , followed the procedures described in
227 Ferreira et al. (2020) and Bastiaanssen et al. (2002), respectively, but with input data from the
228 Moderate-Resolution Imaging Spectroradiometer (MODIS) sensor. H was calculated following the
229 methods described in Table 2: using rah and dT , both traditionally applied in SEB models, but also
230 focusing on peculiarities of SDTF that have never been considered in other SEB models. In this
231 proposed version, rah was described according to Verhoef et al. (1997a) and Paul et al. (2013),
232 which requires, among other parameters/variables, the momentum roughness length ($z0m$), the zero
233 plane displacement height ($d0$), the dimensionless parameter kB^{-1} , and the atmospheric stability
234 corrections (Paulson, 1970). $z0m$ is influenced by a range of plant structural properties, e.g.
235 vegetation height, breadth and vegetation drag coefficients, and spacing (or density). $z0m$ is
236 commonly computed as a function of Leaf Area Index (LAI; Verhoef et al., 1997b; Liu et al., 2021).
237 However, most SDTF plants spend a substantial part of the year without leaves; under these
238 conditions, $z0m$ should be derived from information on dimensions of trunks, stems, and branches.
239 Since LAI is only related to leaf cover quantity and variability, it cannot represent the woody plant
240 structure without leaves (Miranda et al., 2020). Therefore, the Plant Area Index (PAI), which is the
241 total above-ground plant area, i.e. leaves and woody structures, was used to represent plant
242 structures in the computation of $z0m$ and $d0$.

243 To incorporate the conditions of water variability in the forest system in the calculation of
244 sensible heat we applied the procedure described in Gokmen et al. (2012) that corrects the kB^{-1}

245 equation presented in Su et al. (2001), incorporating soil moisture obtained by remote sensing. The
 246 decrease of kB^{-1} with a rise in plant water stress is based on general plant physiological observations
 247 related to vertical canopy stomatal conductance profiles, which affects the exchange of sensible and
 248 latent heat between the canopy and the atmosphere. Thus, when there is a reduction in soil moisture,
 249 there is also a reduction in the value of rah and, consequently, an increase of H and a decrease in
 250 λET . Furthermore, to calculate dT , we used the linear relationship on LST, using the assumption of
 251 extreme contrast in terms of cover and soil wetness (hot/dry and cold/wet endmembers) to determine
 252 the linear relationship coefficients. However, in the hot/dry and cold/wet endmembers pixels, H was
 253 computed by the surface energy balance (Allen et al., 2007), and the remaining λET was
 254 incorporated through the Priestley-Taylor (1972) equation and plant physiological constraints
 255 following the approach in Singh and Irmak (2011) and French et al. (2015). The references for the
 256 methods and equations adopted to formulate the STEEP model can be found in Table 2 and
 257 Appendix A, respectively. For illustration purposes, Table 2 also shows the references for the
 258 methods for one of the most widely used RS SEB models, the SEBAL model.

259 Table 2. References for the methods used in the STEEP and SEBAL models to obtain the sensible
 260 heat flux.

Variable/Parameter	STEPP	SEBAL
Aerodynamic resistance for heat transfer (rah)	Verhoef et al., 1997a; Paul et al., 2013	Bastiaanssen et al., 2002; Laipelt et al., 2021
Roughness length for momentum transfer ($z0m$)	Verhoef et al., 1997b; Paul et al., 2013, replacing LAI with PAI	Bastiaanssen et al., 2002; Laipelt et al., 2021
Zero plane displacement height ($d0$)	Verhoef et al., 1997b; Paul et al., 2013	-
Plant Area Index (PAI)	Miranda et al., 2020	-
Parameter kB^{-1}	Su et al., 2001	uses $z0h$ with constant value (0.1); Bastiaanssen et al., 2002
Correction of soil moisture by remote sensing in kB^{-1}	Gokmen et al., 2012	-
Calculation of the H and the remaining λET in endmembers pixels	Allen et al., 2007; Singh and Irmak, 2011; French et al., 2015	Calculation of the H in the hot/dry endmember only; Bastiaanssen et al., 2002

261

262 2.3 Algorithm implementation and processing

263 We implemented STEEP on the Google Earth Engine (GEE) cloud computing environment
 264 (Gorelick et al., 2017) using the Python API (version 3.6). Statistical analyses to evaluate the
 265 performance of the models were also conducted in Python and implemented in the Jupyter
 266 programming environment. The Python package geemap (Wu, 2020) enabled the integration of
 267 Python with the GEE environment, and the hydrostats package (Roberts et al., 2018) was used for
 268 the statistical evaluation of the performance of the models.

269 We designed the application of the model to take advantage of the data available on GEE
 270 (Table 3). The remote sensing datasets were derived from MODIS sensor products, the Shuttle
 271 Radar Topography Mission (SRTM; Farr et al., 2007), and the Global Forest Canopy Height product
 272 provided vegetation height (Potapov et al., 2021). The climate data necessary to run the model, i.e.,
 273 wind speed, air temperature, relative humidity, shortwave radiation, and net thermal radiation at the
 274 surface, were sourced from the ERA5-Land reanalysis product (Muñoz Sabater, 2019). For data
 275 regarding soil moisture, we used the Global Land Data Assimilation System (GLDAS) product
 276 (Rodell et al., 2004). CHIRPS precipitation product (Funk et al., 2015) was used to estimate the daily
 277 rainfall amount at the sites evaluated.

278 Table 3. Description of the datasets available on the GEE platform used in the research.

Product	GEE ID	Bands/variables	Time coverage	Spatial resolution	Temporal resolution
MCD43A4.006	MODIS/006/ MCD43A4	B1–B7	Feb 2000– present	0.5 km	1 day
MOD09GA.006	MODIS/006/ MOD09GA	SolarZenith	Feb 2000– present	1 km	1 day
MOD11A1.006	MODIS/006/ MOD11A1	LST_Day_1km; Emis_31, Emis_32	Mar 2000– present	1 km	1 day
SRTM	USGS/SRT MGL1_003	Elevation	Feb 2000	0.03 km	-
ERA5-Land	ECMWF/ER A5_LAND/H OURLY	dewpoint_temperature_2m, temperature_2m, u_component_of_wind_10m, v_component_of_wind_10m, surface_net_solar_radiation _hourly, surface_net_thermal_radiati on_hourly	Jan 1981– present	0.1°	1 hour

GLDAS	NASA/GLDA S/V021/NOA H/G025/T3H	SoilMoi0_10cm_inst	Jan 2000– present	0.25°	3 hours
Global Forest Canopy Height, 2019	users/potapo vpeter/GEDI _V27	-	Apr 2019	0.03 km	-
CHIRPS	UCSB- CHG/CHIRP S/DAILY	Precipitation	Jan 1981– present	0.05°	1 day
MOD16A2.006	MODIS/006/ MOD16A2	ET	Jan 2001– present	0.5 km	8 days
PML_V2	projects/pml _evapotrans piration/PML /OUTPUT/P ML_V2_8da y_v016	Es, Ec, Ei	Feb 2000– present	0.5 km	8 days

279

280

281

282

283

284

285

286

287

288

289

290

291

292

293

294

295

296

297

The presence of clouds or instrumental malfunctioning of orbital sensors can cause gaps in data. To reduce the loss of information due to missing data, we chose to use the MODIS MCD43A4 reflectance product. By combining reflectance data from MODIS sensors aboard the AQUA and TERRA satellites and modelling the anisotropic scattering characteristics using sixteen-day quality observations, the MCD43A4 product represents the daily dynamics of the Earth's surface without missing data (Schaaf and Wang, 2015). Daily surface reflectance data from the MCD43A4 product were used to obtain the surface albedo and vegetation indices needed to run STEEP. Thus, the surface albedo data and the vegetation indices show a low percentage of missing data. To compose the LST time series, we used data from MOD11A1, and to fill its missing data, a filter with the average value for a monthly window was applied. This procedure is similar to the method proposed by Zhao et al. (2005) and it is also used by the MOD16 algorithm to generate the continuous global ET (Mu et al., 2011).

Following the approach in comparable studies, STEEP algorithm processing was conducted with automatic selection of endmembers pixels (Bhattarai et al., 2017; Silva et al., 2019; Laipelt et al., 2021). Like Silva et al. (2019), we used the biophysical variables NDVI, surface albedo and LST to automate selection of the endmembers, but we applied different criteria. For the hot/dry endmember selection, the first step consisted of selecting those pixels whose surface albedo values are between the 50 and 75% quantiles, and with NDVI values greater than 0.1 and less than the

298 15% quantile. After this first selection, a refinement is applied by selecting only those pixels from this
 299 first set that have LST values between the 85 and 97% quantiles. Using the set of pixels that met
 300 these criteria, the median values of R_n , G , LST and rah were calculated to establish a single value
 301 for each variable and describe the characteristics of the hot pixel. We applied a similar procedure to
 302 select the cold/wet endmember but with different limits (Table 4). The procedure for finding
 303 endmembers was conducted daily. To execute the model and conduct the selection of endmembers,
 304 we used an area of interest (AOI), also known as domain size. AOI was defined as a square area
 305 with 1000-km sides within the Caatinga domain and centred on the tower coordinates of each site.
 306 Cheng et al. (2021), for example, applied the SEBAL using MODIS data in China and used an AOI
 307 of 1200-km x 1200-km.

308 Table 4. Methodology used for the selection of endmembers pixels.

Endmembers		
	Hot/dry pixel	Cold/wet pixel
Step 1	Q50% < surface albedo < Q75% and 0.10 < NDVI < Q15%	Q25% < surface albedo < Q50% and NDVI > Q97%
Step 2	of the pixels of the 1st Step, select pixels with Q85% < LST < Q97%	of the pixels of the 1st Step, select pixels with LST < Q20%
Step 3	Of the set of pixels that met the previous steps, the median values of R_n , G , LST and rah were calculated to establish a single value for each variable and describe the characteristics of endmembers	

309 Q = quantile.

310 2.4 Analysis of the algorithms' performance

311 We used SEBAL as a reference RS SEB model for comparison with STEEP. SEBAL is one
 312 of the most applied SEB models since the algorithm uses a minimal number of in situ measurements
 313 compared to similar models, e.g. METRIC and SSEBop, and is considered a suitable choice for
 314 evapotranspiration estimates over cropped areas and in the context of water resource management
 315 (Kayser et al., 2022). Applications with SEBAL have been conducted in the Caatinga as in the studies
 316 of Teixeira et al. (2009), Santos et al. (2020), Costa et al. (2021), and Lima et al. (2021).
 317 Implementations of the SEBAL algorithm are popular on several computing platforms, e.g. GRASS-
 318 Python (Lima et al., 2021); Google Earth Engine (Laipelt et al., 2021); Python (Mhawej et al., 2020),
 319 following the formulations described in Bastiaanssen et al. (1998) and Bastiaanssen et al. (2002).
 320 The SEBAL version implemented in this work followed those presented by Bastiaanssen et al.

321 (2002), Costa et al. (2021) and Laipelt et al. (2021). The remote sensing datasets and endmembers
322 pixels selection for SEBAL were the same as described in STEEP.

323 ET and H estimates from STEEP and SEBAL were evaluated against the eddy covariance
324 measurements of the corresponding tower. Here, the modelled values were extracted for the pixel
325 representing the EC tower for each observation site. We did not compute the footprint of the
326 observation sites to determine the size of the influence of each measurement due to the spatial
327 resolution of MODIS products being 0.5 km or greater (Biggs et al., 2016). We evaluated daily ET
328 values, and instantaneous hourly H values more specifically with the modelled/measured H value at
329 11:00 am local time (GMT-3), considering this is the closest time to the satellite's overpass.
330 Additionally, the STEEP model was compared with two consolidated global ET products available
331 on GEE: MODIS Global Terrestrial Evapotranspiration A2 version 6 (MOD16; Mu et al., 2011;
332 Running et al., 2017) and Penman-Monteith-Leuning model version 2 global evaporation (PMLv2;
333 Zhang et al., 2019); both products have a pixel resolution of 500 m (Table 3). The algorithm used in
334 MOD16 is based on the Penman-Monteith equation and driven by MODIS remote sensing data with
335 Modern-Era Retrospective analysis for Research and Applications (MERRA; Mu et al., 2011). In
336 MOD16 ET is the sum of soil evaporation (E_s), canopy transpiration (T_c) and wet-canopy evaporation
337 (E_c) and is provided as eight-day *cumulative* values. More details about MOD16 can be found in Mu
338 et al. (2011) and Running et al. (2017). The global PMLv2 product involves a biophysical model
339 based on the Penman-Monteith-Leuning equation which also uses MODIS remote sensing data, but
340 with meteorological reanalysis data from GLDAS as model inputs. As in MOD16, ET in PMLv2 is
341 also the sum of E_s , T_c and E_c but is provided as eight-day *average* values. To make MOD16 and
342 PMLv2 values compatible, ET of PMLv2 was multiplied by eight. Details about PMLv2 can be found
343 in Gan et al. (2018) and Zhang et al. (2019). We accumulated the daily ET measured at the
344 observation sites, i.e. derived from EC data, and ET modelled with STEEP for the same eight-day
345 time periods to make them compatible with the temporal resolution of the MOD16 and PMLv2
346 datasets. The average of the measured daily values over each eight-day time period (even if there
347 were missing values within this period) was multiplied by eight to calculate the observed 8-day ET.
348 To match the time steps of STEEP and MOD16/PMLv2 ET values, the 8-day average of the
349 evaporative fraction (EF) was multiplied by the daily net radiation over those 8 days, assuming that

350 EF can be considered constant in each of these periods. Then the ET was summed over the 8-day
 351 interval. Finally, we also compared the modelled ET (by STEEP and the two global products) with
 352 the observed ET, only in the 8-day periods when no field-observed data was missing. However, with
 353 this criterion the number of observations dropped dramatically.

354 The STEEP and SEBAL models and global ET products were evaluated with five
 355 performance metrics (Table 5). A combination of performance metrics is often used to assess the
 356 overall performance of models because a single metric provides only a projection of a certain aspect
 357 of the error characteristics (Chai and Draxler, 2014). Root mean square error (*RMSE*) is commonly
 358 used to express the accuracy of the results with the advantage that it presents error values in the
 359 same units of the variable analysed; optimal values are close to zero (Hallak and Pereira Filho,
 360 2011). Coefficient of determination (R^2) represents the quality of the linear trend between observed
 361 and simulated data and ranges from 0 to 1; high values indicate better model performance. Nash–
 362 Sutcliffe efficiency (*NSE*) indicates the accuracy of the model output compared to the average of the
 363 referred data ($NSE = 1$ is the optimal value; Nash and Sutcliffe, 1970). Concordance correlation
 364 coefficient (ρ_c) is a measure that evaluates how well bivariate data falls on the 1:1 line. ρ_c measures
 365 both precision and accuracy. It ranges from -1 to +1 similar to Pearson's correlation coefficient, with
 366 perfect agreement at +1 (Lin, 1989; Liao and Lewis, 2000; Akoglu, 2018). Percentage bias (*PBIAS*)
 367 measures the average relative difference between observed and estimated values, with an optimal
 368 value of 0 (Gupta et al., 1999).

369 Table 5. Performance metrics used to evaluate ET and *H* in this study.

Performance metric	Equation	Range (Perfect value)
Root mean square error (<i>RMSE</i>)	$RMSE = \sqrt{\frac{\sum_{i=1}^N (M_i - O_i)^2}{N}}$	[0, +∞ [(0)
Coefficient of determination (R^2)	$R^2 = \frac{[\sum_{i=1}^N (O_i - \bar{O})(M_i - \bar{M})]^2}{\sum_{i=1}^N (O_i - \bar{O})^2 \cdot \sum_{i=1}^N (M_i - \bar{M})^2}$	[0, 1] (1)
Nash–Sutcliffe efficiency (<i>NSE</i>)	$NSE = 1 - \frac{\sum_{i=1}^N (M_i - O_i)^2}{\sum_{i=1}^N (O_i - \bar{O})^2}$]-∞, 1] (1)
Concordance correlation coefficient (ρ_c)	$\rho_c = \frac{2 \sum_{i=1}^N (O_i - \bar{O})(M_i - \bar{M})}{\sum_{i=1}^N (O_i - \bar{O})^2 + \sum_{i=1}^N (M_i - \bar{M})^2 + (N - 1)(\bar{O} - \bar{M})^2}$	[-1, 1] (1)

Percentage bias (<i>PBIAS</i>)	$PBIAS = \frac{\sum_{i=1}^N (M_i - O_i) \cdot 100}{\sum_{i=1}^N O_i}$] $-\infty, +\infty$ [(0)
-------------------------------------	---	----------------------------

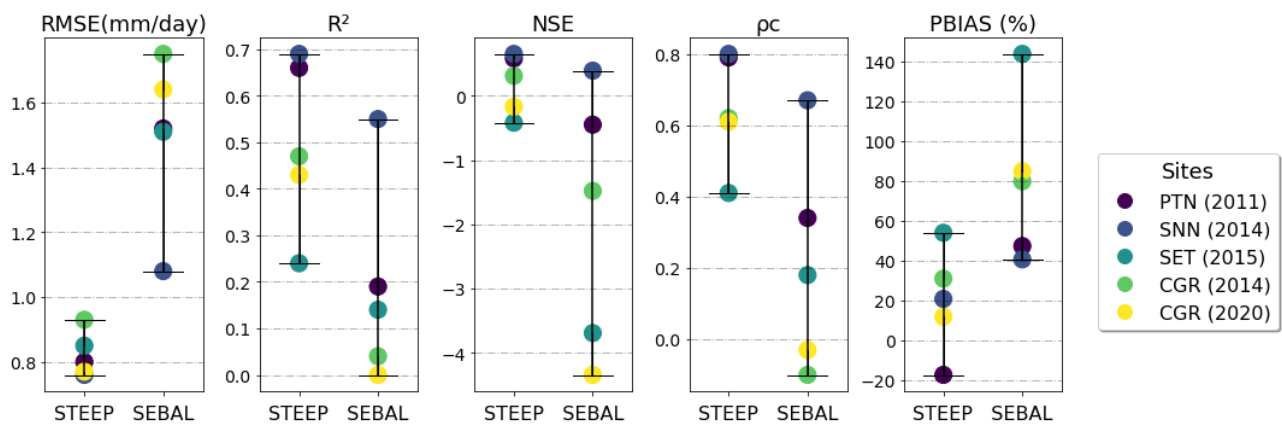
370 where: *N* sample size; *O* observed value; *M* modelled value; \bar{O} observed mean; \bar{M} modelled mean.

371 **3. Results and discussion**

372 3.1 Comparison of STEEP and SEBAL models results with observed (EC) values

373 STEEP exhibited better statistical performance than SEBAL at all the evaluated sites (Fig.
 374 2). While STEEP exhibited a *RMSE* between 0.75 and 0.94 mm/day, the *RMSE* for SEBAL was
 375 between 1.08 and 1.75 mm/day. In terms of *R*², the values were between 0.24 to 0.69 for STEEP,
 376 and were below 0.2 for SEBAL for all sites except in SNN (0.55). Similarly, *NSE* and *ρc* values were
 377 higher for STEEP compared to SEBAL. For STEEP, all sites had *NSE* and *ρc* values above -0.42
 378 and 0.41, respectively, whereas all sites except SNN had values below these limits for SEBAL. Both
 379 models overestimated ET (*PBIAS* > 0), with the exception of the STEEP estimates for the PTN site.
 380 The highest overestimation by the STEEP model was less than 60%, whereas in SEBAL it was
 381 greater than 140%.

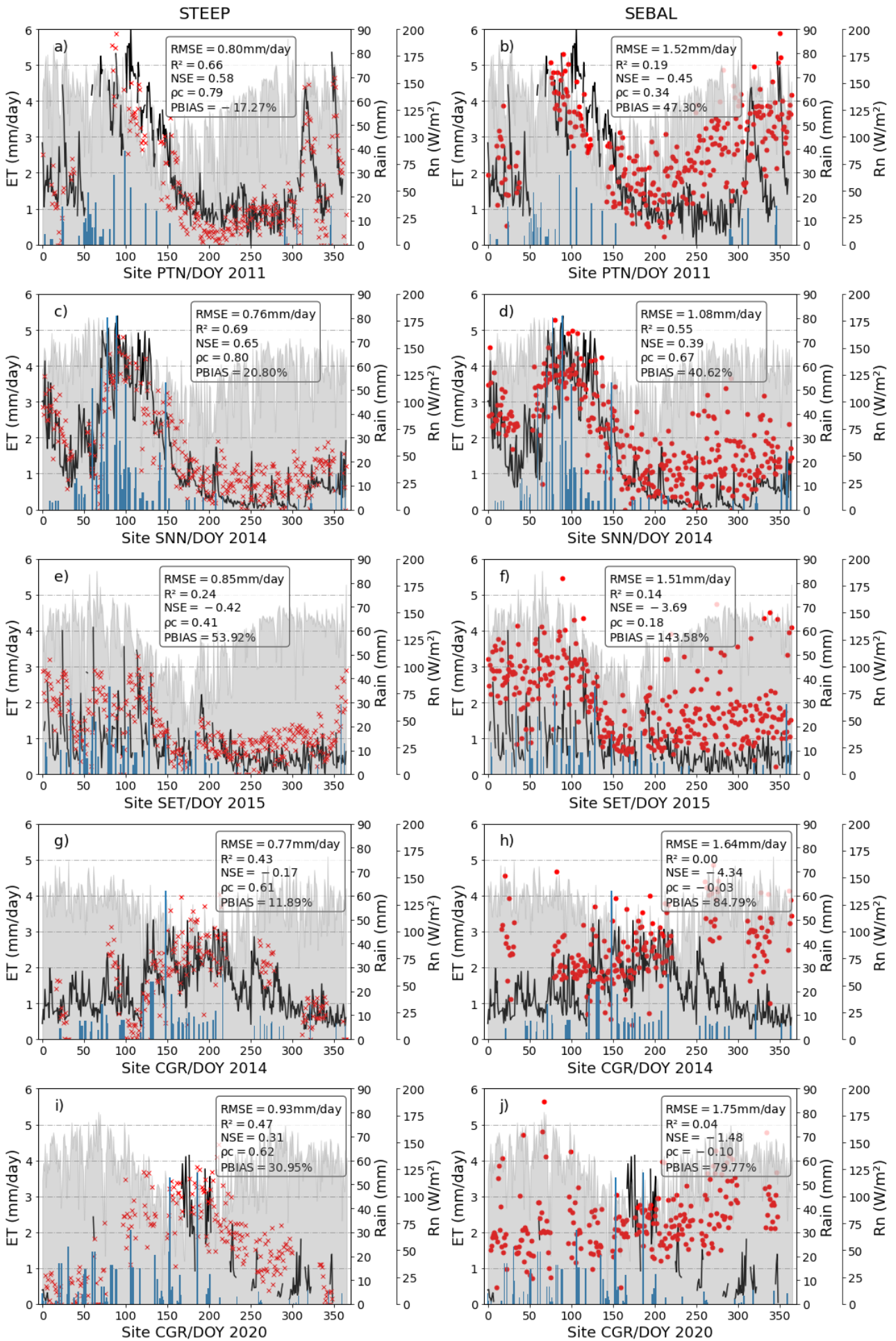
382 SEBAL metrics concerning the modelled ET were similar to those found in other studies.
 383 Laipelt et al. (2021) found *R*² ranging from 0.18 to 0.87 when applying SEBAL and comparing it with
 384 data from ten EC towers located in different Brazilian biomes (Amazon, Cerrado, Pantanal, and
 385 Pampa). Cheng et al. (2021) obtained *R*² of 0.53–0.77 and *RMSE* of 0.89–1.02 mm/day when
 386 comparing estimates from SEBAL and EC towers on different land covers in China. Costa et al.
 387 (2021), when applying SEBAL in the Caatinga, found *R*² and *NSE* values of 0.57 and 0.36,
 388 respectively. Santos et al. (2020) modelled ET with SEBAL at the SNN site for the 2014–2016 period
 389 and obtained *R*² and *RMSE* values of 0.28 and 1.43 mm/day, respectively. For this site, we obtained
 390 *R*² and *RMSE* of 0.55 and 1.08 mm/day, respectively, for the year 2014 using SEBAL.



392 Figure 2. Results of the performance statistics of daily ET for evaluated sites.

393 STEEP exhibited a greater seasonal accuracy compared to SEBAL (Fig. 3), as evidenced by
 394 the goodness-of-fit between simulated and observed values expressed by the *NSE* indicator (Fig.
 395 2). STEEP estimates followed the same temporal evolution as the observed values. STEEP
 396 satisfactorily captured both minimum and maximum ET values, including after rainfall events, this is
 397 particularly evident in Fig. 3a, where the two observed ET peaks in late 2011 — between DOY 300
 398 and 360 — in the PTN site were captured nicely by STEEP. This improved performance can be
 399 explained because soil moisture is incorporated in the STEEP algorithm. In semi-arid regions and
 400 particularly in the SDTF, besides the availability of energy, evapotranspiration is highly dependent
 401 on the soil–water availability (Lima et al., 2012; Carvalho et al., 2018; Mutti et al., 2019; Paloschi et
 402 al., 2020). In rainy months, low daily ET rates are often observed due to the reduced levels of
 403 incoming radiation caused by high cloud cover (Mutti et al., 2019; Paloschi et al., 2020). Towards
 404 the end of the wet period, when the available energy increases, the daily ET values also increase as
 405 a result of the high soil water availability from previous precipitation events (Allen et al., 2011;
 406 Marques et al., 2020). In the transition period from the rainy to the dry season, the leaves do not fall
 407 immediately. Instead, leaf-shedding depends on the environmental conditions in each location,
 408 including the rainy season duration, and species composition (Lima and Rodal, 2010; Lima et al.,
 409 2012; Miranda et al., 2020; Paloschi et al., 2020; Queiroz et al., 2020; Medeiros et al., 2022). The
 410 remaining water available in the soil or previously accumulated in plant tissues is sufficient for the
 411 Caatinga vegetation to maintain its leaves, for short periods, at levels similar to the rainy season
 412 (Barbosa et al., 2006; Mutti et al., 2019). However, in the dry season, when soil moisture reaches its
 413 lowest levels, the Caatinga vegetation enters a state of dormancy that is accompanied by leaf drop

414 and a drastic reduction of photosynthetic activity (and hence of transpiration) as a strategy to cope
415 with the lack of available soil moisture (Dombroski et al., 2011; Paloschi et al., 2020). This resilience
416 mechanism is typical of xerophytic and/or deciduous species such as those found in the Caatinga
417 (Lima et al., 2012; Mutti et al., 2019; Paloschi et al., 2020), and explains the low rates of ET in the
418 dry season. In contrast, in SEBAL, which does not consider water availability, it was observed that
419 the daily ET followed the course of the daily net radiation throughout the year, especially in the dry
420 period of each of the experimental sites. This is in agreement with the results of Kayser et al. (2022),
421 who pointed out that estimates with SEBAL can be seasonally accurate in locations where the main
422 driver of ET is the available energy. Our results highlight that SEB models such as SEBAL, which
423 are formulated to be mainly dependent on energy availability and do not consider soil and plant water
424 availability, may not satisfactorily represent ET in semi-arid vegetation such as that found in the
425 SDTF (Gokmen et al., 2012; Paul et al., 2014; Melo et al., 2021).

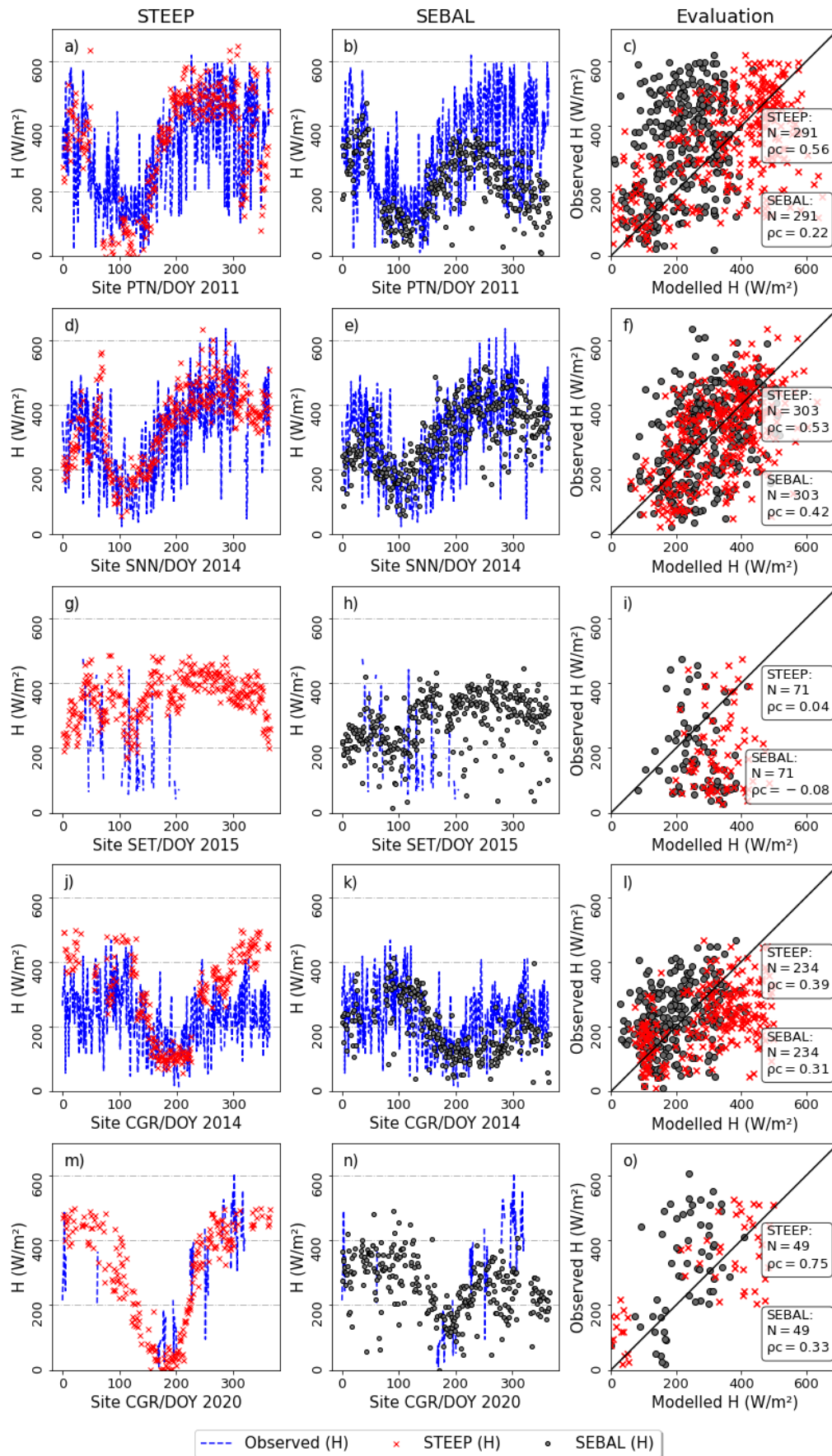


— Observed ET × STEEP • SEBAL ■ RAIN - CHIRPS ■ Daily net radiation

427 Figure 3. Observed and modelled daily evapotranspiration (ET, mm/day) for the different
428 experimental sites: a) and b) PTN 2011, c) and d) SNN 2014, e) and f) SET 2015, g) and h) CGR
429 2014, i) and j) CGR 2020. The black lines represent observed ET; the red crosses and points are
430 STEEP and SEBAL estimates, respectively; the blue bars represent CHIRPS daily rainfall; the gray
431 region represents daily net radiation from ERA5-land.

432 The core of the STEEP and SEBAL algorithms is based on finding λET as the residual of the
433 energy balance; however, they differ with regards to the approach used to calculate H . In the STEEP
434 model, the seasonal variation of H fitted the observed values of the instantaneous measurements at
435 11:00 am (local time) better than SEBAL, for all the sites (Fig. 4). While STEEP estimates of H
436 exhibited ρc values over 0.5 for three of the five sites, SEBAL H estimates exhibited ρc values below
437 0.5 for all sites.

438



439

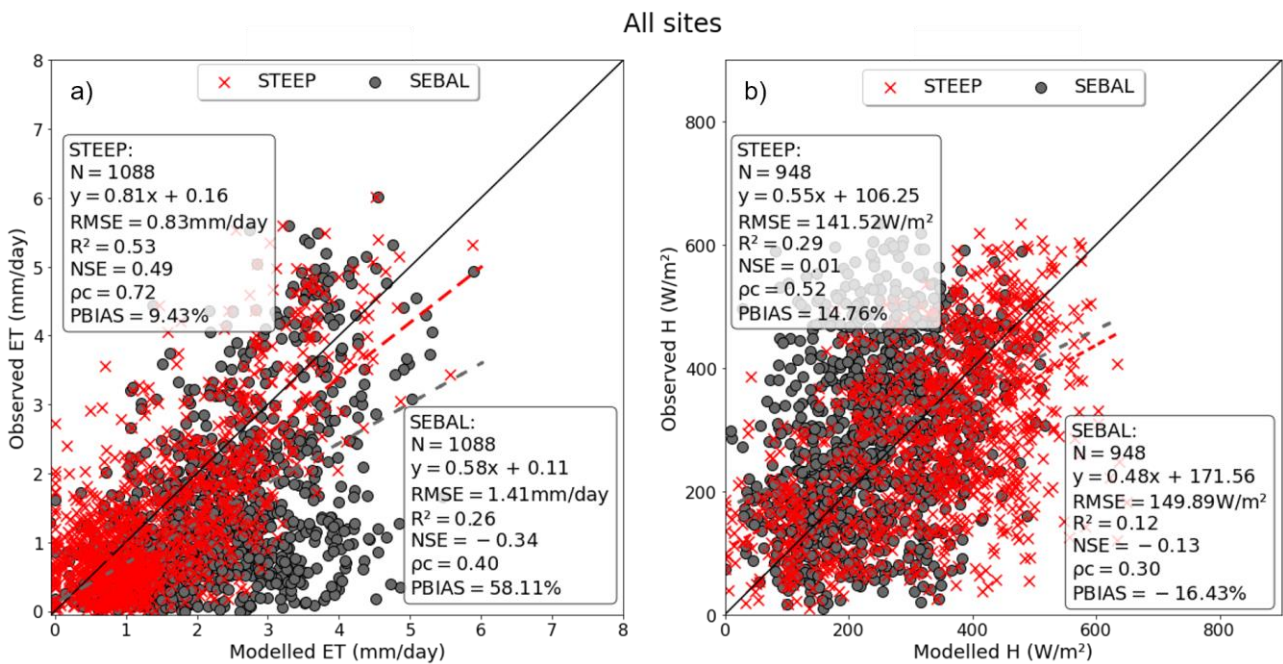
440

441

Figure 4. Observed and modelled instantaneous sensible heat flux (H , at 11:00 am, W/m²) for the different experimental sites: a), b) and c) PTN 2011, d), e) and f) SNN 2014, g), h) and i) SET

442 2015, j), k) and l) CGR 2014, m), n) and o) CGR 2020. The blue line represents the observed
 443 values; the red crosses and grey points correspond to the STEEP and SEBAL estimates,
 444 respectively. The black line is the 1:1 line.

445 Evaluation of the STEEP and SEBAL daily ET and instantaneous H for all experimental sites
 446 (Fig. 5) indicates that both models lack a high performance for H estimates, although the use of
 447 STEEP resulted in better statistical measures than when SEBAL was employed (Fig. 5b). It can be
 448 seen that the overestimation of H by the STEEP model, compared to SEBAL, produced modelled
 449 ET values that were closer to the EC measurements. This may indicate that either R_n was
 450 overestimated or G underestimated in the RS SEB methods, or that there was a lack of energy
 451 balance closure in the EC measurements.



452
 453 Figure 5. Evaluation of observed and modelled: (a) daily evapotranspiration (ET, mm/day) and b)
 454 instantaneous sensible heat flux (H , at 11:00 am, W/m²) for all experimental sites. STEEP (red
 455 crosses) and SEBAL (black points). The black line is the 1:1 line; the red (gray) dashed line is the
 456 fitted linear regression between observed and STEEP (SEBAL) model values.

457 We attribute the better performance of STEEP over SEBAL for the Brazilian Caatinga to at
 458 least three reasons. First, roughness characteristics near the surface where the heat fluxes originate
 459 are parameterised by z_{0m} , which depends on several factors, such as wind direction, height and
 460 type of the vegetation cover (Kustas et al., 1989). Estimation of z_{0m} only with an exponential

461 relationship, as a function of vegetation indices, may be an oversimplification (Kustas et al., 1989;
462 Paul et al., 2013). In our study, z_{0m} and d_0 are calculated using PAI instead of LAI and with the
463 equations proposed in Verhoef et al. (1997b). This procedure considers the characteristics of SDTF,
464 such as seasonality of phenology and vegetation height, that considerably affect the quantification
465 of turbulent transfer (Liu et al., 2021). Secondly, our study uses the equation described in Verhoef
466 et al. (1997a) and Paul et al. (2013) to estimate rah , which considers the differences between heat
467 and momentum transfer, unlike the original equation employed in other SEB models e.g. SEBAL or
468 METRIC that only considers z_{0m} and $z_{0h} = 0.1$ when computing this resistance. Furthermore, we
469 account for the kB^{-1} parameter that varies in space and time and incorporates the soil moisture
470 content obtained by RS (Su et al., 2001; Gokmen et al., 2012). ET estimation is best represented
471 with a spatially varying kB^{-1} value, as pointed out by the studies of Gokmen et al. (2012) and Paul et
472 al. (2014). Third, by quantifying the remaining λET in the endmembers pixels through the Priestley-
473 Taylor equation, a more reliable estimate of H in the endmembers pixels can be obtained, as was
474 also evidenced by Singh and Irmak (2011). This process is critical for the subsequent numerical
475 calculation of H in SEB models that use the dT , as its accuracy is closely related to quantifying the
476 energy balance at the hot and cold endmembers (Trezza, 2006; Allen et al., 2007; Singh and Irmak,
477 2011; Singh et al., 2012).

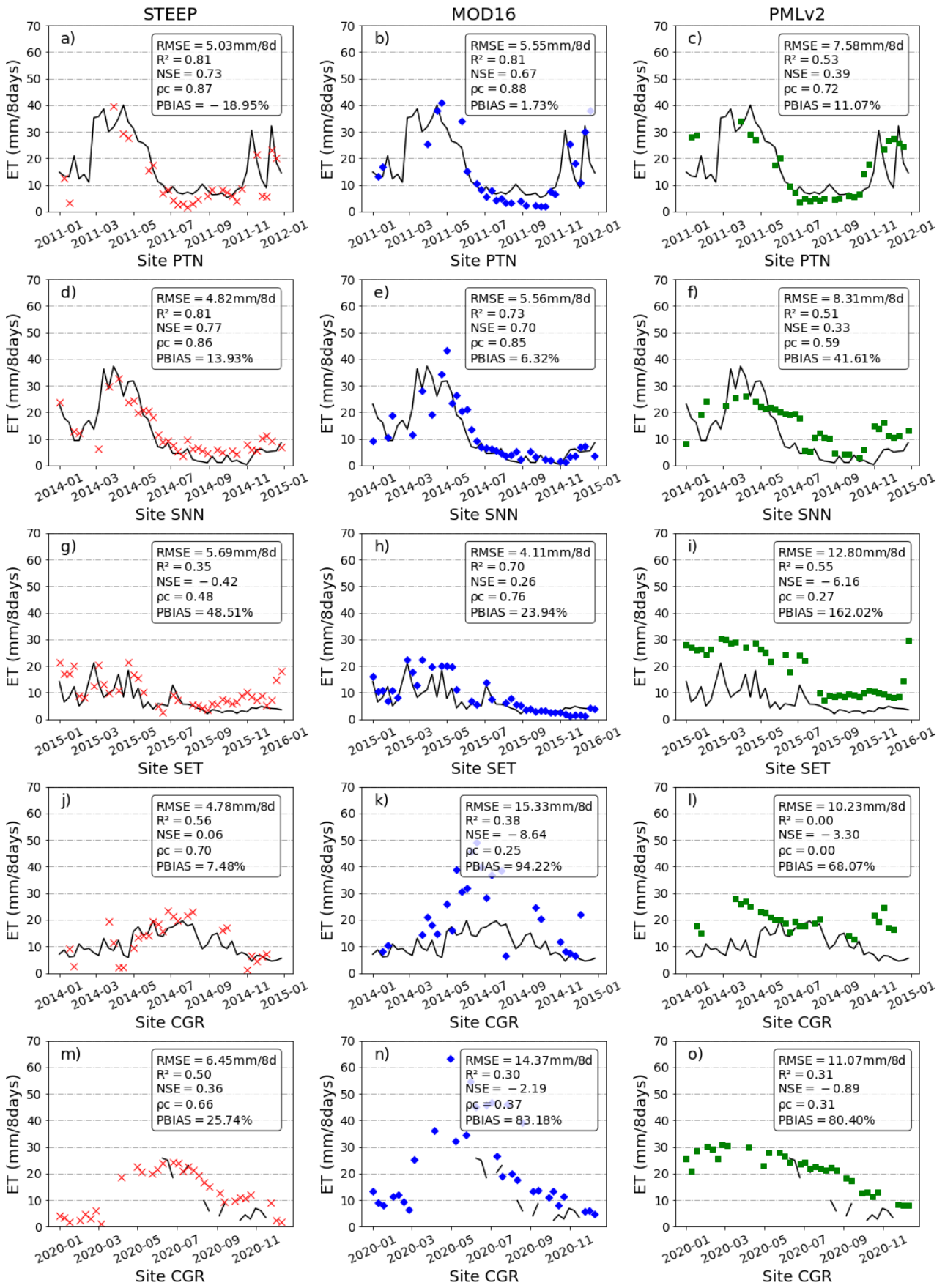
478 The impact on the performance metrics of each proposed refinement of the STEEP model
479 (methods for z_{0m} , rah and remaining λET in the endmembers pixels), and of their two by two
480 combinations were analysed. We run the control version of the SEB model (SEBAL in our case)
481 while incorporating one or two improvements in the model and keeping the remaining parts of the
482 algorithm the same as the reference SEB model. The results (Table S1) show that including just one
483 or two of the refinements had only partial performance gains. In contrast, all the proposed STEEP
484 improvements implemented together resulted in the best performance metrics for all sites.

485 3.2 Comparison of STEEP model estimates with global evapotranspiration products

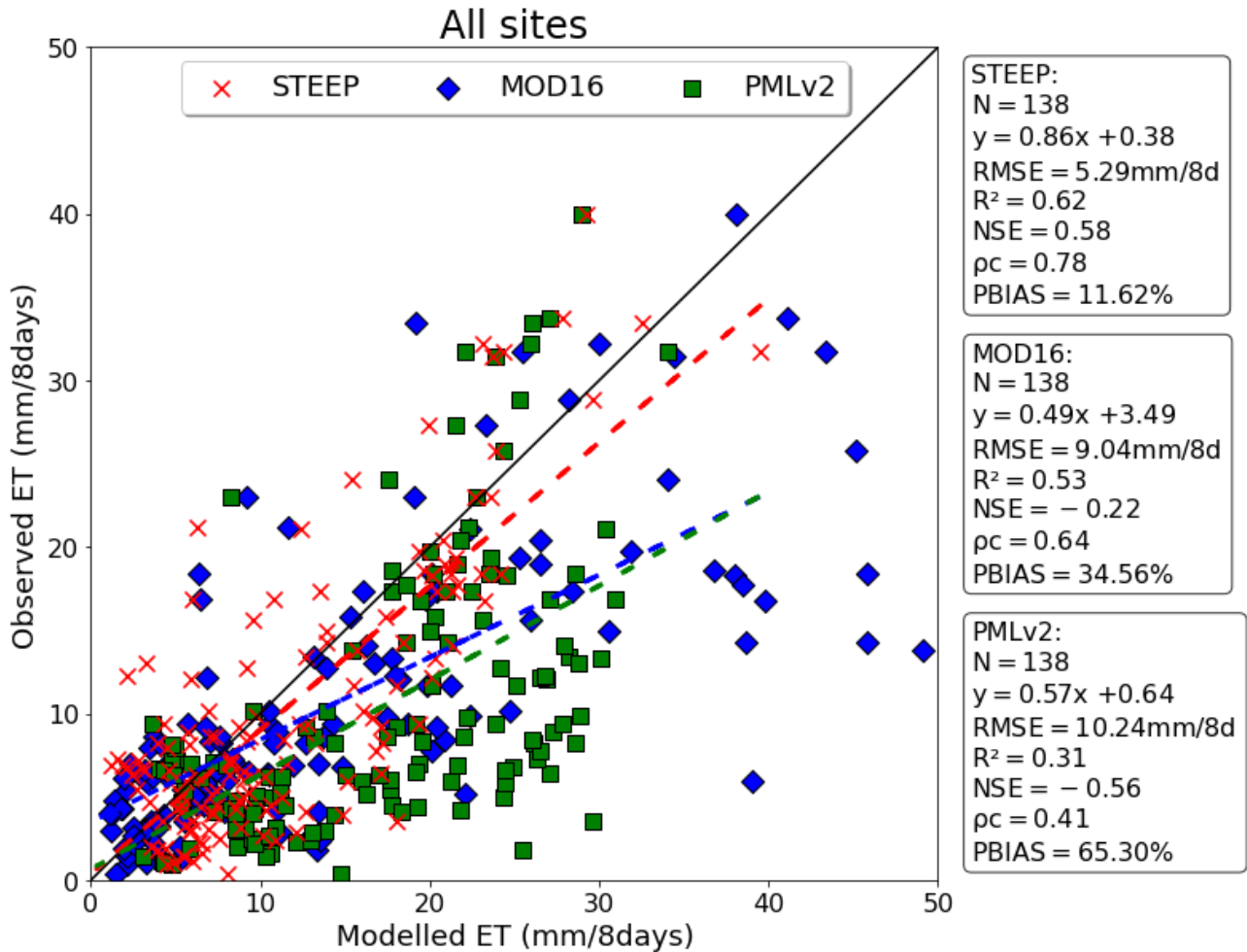
486 The comparison of ET estimates by STEEP, MOD16 and PMLv2 with the observed values
487 at the different sites (Fig. 6) reveals that the ET estimates by STEEP and global products adequately
488 followed the seasonality of the values, with a better fit for STEEP and MOD16. In general, the
489 evaluation at the different sites shows that the $RMSE$ of STEEP was not higher than 6.45 mm/8

490 days, while the ET products' maximum *RMSE* was close to 15 mm/8 days. It is noted that the lowest
491 *RMSE* value found (4.11 mm/8 days) was for MOD16 at the SET site. Regarding R^2 values, 80% of
492 the evaluations with STEEP were equal to or greater than 0.50. For MOD16, 60% of the R^2 values
493 were equal to or greater than 0.70, while for PMLv2, no site had R^2 values that exceeded 0.55. The
494 best *NSE* value produced by STEEP was 0.77, while with MOD16, it was 0.70, both at the SNN site,
495 while PMLv2 did not exceed 0.39 (PTN site). Regarding ρ_c , the percentages of ET evaluations that
496 obtained values equal to or greater than 0.70 were 60% for STEEP and MOD16, and only 20% for
497 PMLv2 (site PTN). The overestimations (*PBIAS*) with STEEP were not higher than 50%, and not
498 higher than 95% with MOD16. For PMLv2 the overestimations did not exceed 80%, except for the
499 SET site that obtained a *PBIAS* of 150%. We highlight the good performance of MOD16 for the SET,
500 SNN, and especially the PTN sites, with very good performance metrics and seasonal behaviour,
501 capturing ET values in dry periods very well. The evaluation results of STEEP, MOD16 and PMLv2
502 for all observation sites combined are shown in Fig. 7. Noteworthy is the better performance of
503 STEEP over MOD16 and PMLv2, with *RMSE* < 6 mm/8 days, R^2 and *NSE* greater than or close to
504 0.60, $\rho_c > 0.75$ and an average overestimation < 12%. Analysis with the dataset considering only
505 the 8-day time periods without missing field-observed data, i.e. periods with valid ET measurements
506 during eight consecutive days (Fig. S1) did not change the results overall, confirming STEEP's
507 dominance compared to the two standard products evaluated.

508



510 Figure 6. Temporal evolution of ET from STEEP, MOD16 and PMLv2 for the different observation
 511 sites, and their individual performance statistics. a), b) and c) PTN 2011; d), e) and f) SNN 2014; g)
 512 h) and i) SET 2015; j), k) and l) CGR 2014; m), n) and o) CGR 2020. Black lines correspond to
 513 observed ET while data points refer to estimates by the STEEP model (red crosses), MOD16 (blue
 514 diamonds) and PMLv2 (green squares) products.



515
 516 Figure 7. Evaluation of evapotranspiration (ET, mm/8days) observed and modelled with STEEP
 517 (red crosses), MOD16 (blue diamonds) and PMLv2 (green squares) for all experimental sites. The
 518 black line is the 1:1 line; dashed lines are the fitted linear regressions of observed versus modelled
 519 values by the STEEP model (red), MOD16 (blue) and PMLv2 (green) products.

520 The explanation of the differences between STEEP and the MOD16 and PMLv2 products is
 521 two-fold. Firstly, the way ET is obtained differs between STEEP and the other products. While
 522 STEEP and other SEB single-source models estimate ET as a combined singular process, i.e., there
 523 is no distinction between soil evaporation and transpiration (Sahnoun et al., 2021) and interception

524 loss is not taken into account, MOD16 and PMLv2 discriminate the components of soil evaporation,
525 canopy transpiration, and wet canopy evaporation (Mu et al., 2011; Zhang et al., 2019). With this in
526 mind it is remarkable that STEEP performs better than the other, widely used, multiple-source ET
527 products. Secondly, the input data sets and their uses are different. The driving meteorological data
528 for STEEP are from ERA5-Land, while in MOD16, they are from MERRA and in PMLv2 are provided
529 by GLDAS (Mu et al., 2011; Zhang et al., 2019). In addition, the meteorological elements used are
530 different among the ET products. MOD16 requires air temperature, atmospheric pressure, relative
531 humidity, and downward shortwave radiation. In addition to these elements, PMLv2 also requires
532 precipitation, downward longwave radiation, and wind speed (Mu et al., 2011; Zhang et al., 2019;
533 Yin et al., 2020; Chen et al., 2022). Although both ET products use the same land cover data
534 (MOD12Q1), only MOD16 integrates it into its algorithm. In MOD16, the land cover type defines
535 biome delimitation for the characterization of leaf stomatal conductance, vapour pressure deficit
536 (VPD) and other related factors, while PMLv2 only uses land cover to construct a mask of the land
537 area (Chen et al., 2022). The sources and use of LAI in these two products are also different. LAI is
538 used to increase leaf conductance in MOD16, while it is used to divide the total available energy into
539 canopy uptake and soil uptake in PMLv2 (Mu et al., 2011; Zhang et al., 2019; Chen et al., 2022).
540 Although MOD16 uses EC data from 46 distributed sites for validation (Mu et al., 2011) and PMLv2
541 uses EC data from 95 distributed sites and ten plant functional types for calibration (Zhang et al.,
542 2019; Yin et al., 2020), none of the products had observation sites in SDTF.

543 The uncertainties associated with field measurements of ET can also influence the evaluation
544 of the model products. It is generally accepted that EC flux towers provide reliable local, i.e. for areas
545 of relatively limited spatial extensions, ca. 1 km², ET measurements (Mu et al., 2011; Salazar-
546 Martínez et al., 2022). However, generally flux tower data have a lack of energy balance closure,
547 that is the difference between net radiation and ground heat flux is sometimes greater than the sum
548 of the turbulent latent and sensible heat fluxes, an error that can be in the range of 10–30% (Wilson
549 et al., 2002; Foken, 2008; Allen et al., 2011). This gap can result from instrument errors, weather
550 and surface conditions, e.g. those that result in advection, and gap-filling methods (Mu et al., 2011).
551 Although the data from the EC flux towers have been filtered to minimise errors due to lack of SEB
552 closure, their influence cannot be neglected. In addition, the complex and heterogeneous canopy

553 structure, the stochastic nature of turbulence (Hollinger and Richardson, 2005) and adverse weather
554 conditions, e.g. rainy and stormy days, tower sensors recording abnormal values, can affect ET
555 measurements obtained by EC systems (Ramoelo et al., 2014).

556 3.3 Sources of error and further research for STEEP

557 In its current configuration, STEEP has some limitations that should be noted. Meteorological
558 reanalysis provides only large-scale averages and can misrepresent local meteorological conditions;
559 hence, it suffers from biases, especially over heterogeneous surfaces (Rasp et al., 2018; Laipelt et
560 al., 2020). However, despite moderate accuracy and biases at regional scales, ground-based
561 assimilation and reanalysis data have become important sources of meteorological inputs for ET
562 estimates (Mu et al., 2011; Zhang et al., 2019; Allam et al., 2021; Senay et al., 2022). Laipelt et al.
563 (2020) and Kayser et al. (2022) observed that the use of ground measurements or global reanalysis
564 data as meteorological inputs had modest effects only on the accuracy of SEBAL to estimate ET.
565 Also, although gap-filling was used in the present study to improve the availability of LST data, this
566 procedure should be used with caution. In addition, care should be taken when using the MCD43A4
567 reflectance product, because in its composition there is also gap-filling. For example, on some cloudy
568 days, the estimates of vegetation indices, surface albedo and LST may have introduced inaccuracies
569 in the STEEP (and in SEBAL) model calculation process due to these gap-filling methods. Regarding
570 the selection of endmembers pixels, although the temporal evolution of the selected pixels in this
571 study seems plausible, their representativeness of the actual conditions may be debatable,
572 especially considering the considerable extent of the AOI. The computational capacity and the
573 effectiveness of GEE for running SEB models should be commended. Although other studies have
574 demonstrated GEE's strength (Laipelt et al., 2021; Jaafar et al., 2022; Senay et al., 2022), this
575 platform has some limitations when it comes to the number of iterations, e.g. a convergence
576 threshold cannot be set to stop the within-loop iterations of H calculations; instead a fixed number of
577 iterations needs to be defined. Still, the availability of the several necessary datasets within one
578 platform greatly facilitates the run of STEEP and other SEB models.

579 One of the main focuses of this study is to provide a one-source model capable of
580 representing ET in environments that are mainly governed by soil–water availability, such as those
581 represented by SDTF, in a parsimonious way. Based on our findings we deem this main aim to be

582 achieved due to the relative simplicity of the STEEP model and its low data demand. The improved
583 performance of STEEP was the result of improvement of existing and physically meaningful
584 parameters (z_{0m} and kB^{-1}), rather than by introducing additional empirical parameters, thereby
585 satisfying the principle of equifinality (see Beven and Freer, 2001). To explore further the potential
586 and accuracy of STEEP, more research is needed to analyse the impact that the improved H
587 approach has on ET of different land covers at longer time scales. Improving the quantification of
588 regional ET via RS-based SEB models has a great potential to provide a more accurate estimate of
589 the energy and water fluxes in SDTF regions, and will contribute to a better understanding of the
590 water cycle, its uses, and the interrelationships with ecosystem functioning.

591 **4. Conclusions**

592 Our work provides an improved approach for estimating the latent and sensible heat fluxes
593 by remote sensing for land covers that experience seasonally varying severely reduced water
594 availability. We tested it for four SDTF sites. The STEEP model focuses on the special features of
595 the SDTF: the Plant Area Index is used to take into account the woody structure of the plants in
596 calculating the momentum roughness length. In the equations to calculate the aerodynamic
597 resistance for sensible heat transfer (using the bulk heat transfer equation), the parameter kB^{-1} was
598 included, and it was allowed to vary in time as a function of corrected soil moisture, obtained by
599 remote sensing. Finally, the remaining λET in endmembers pixels was quantified using the Priestley-
600 Taylor equation. STEEP estimates for H and ET were evaluated at four observation sites equipped
601 with EC systems in the Caatinga, the largest continuous SDTF in the Americas. The metrics of
602 STEEP for instantaneous estimates of H and daily estimates of ET were compared with estimates
603 from the SEBAL model, and ET at the eight-day scale with the widely used global products MOD16
604 and PMLv2.

605 In summary, the main conclusions are:

- 606 • The estimates of H by STEEP allowed ET estimates to be closer to the observed field
607 values than those obtained by SEBAL. Based on all the performance metrics used to
608 analyse the models, STEEP was superior to SEBAL. STEEP showed $RMSE$ less than
609 1mm/day, R^2 between 0.24 and 0.69, NSE between -0.17 and 0.65, pc between 0.41

610 and 0.80 and *PBIAS* between -17% to 54%. Also noteworthy is how well STEEP captured
611 the seasonal course of observed ET.

612 • Compared with ET data from the global MOD16 and PMLv2 products, the STEEP model
613 simulated a similar but generally superior seasonal evolution and its performance metrics
614 were also better. Considering all observation sites simultaneously, at the eight-day scale,
615 STEEP showed superior performance with *RMSE* less than 6 mm/8days, *R*² and *NSE*
616 equal to or greater than 0.60, *ρc* greater than 0.75, and an overestimation of < 12%.

617 Thus, we conclude that STEEP, a one-source model that incorporated the seasonality of the
618 aerodynamic and surface variables, was well-heeled in representing ET in environments that are
619 mainly governed by soil–water availability. All the same, there is a need to evaluate the newly
620 developed STEEP model performance for different land covers, climate, and for a longer time series
621 not considered during the modelling process in this study.

622 **Acknowledgements**

623 The Coordenação de Aperfeiçoamento de Pessoal de Nível Superior-Brazil (CAPES)-Finance Code
624 001, provided scholarships to the first and fifth authors. This work was funded by the Brazilian
625 National Council for Scientific and Technological Development (CNPq), grant 409341/2021-5, by the
626 Paraíba Scientific Foundation (FAPESQ), under startup grant 010/2021, and by São Paulo Scientific
627 Foundation (FAPESP), grant 2015/24461-2. CEF is a research unit funded by Fundação para a
628 Ciência e a Tecnologia I.P. (FCT), Portugal (UIDB/00239/2020).

629 **Data Availability Statement**

630 ET data for the PTN, SNN, and SET sites were published by Melo et al. (2021), and are available at
631 <https://doi.org/10.5281/zenodo.5549321>. ET data for the CGR site; H data for the PTN, SNN, CGR
632 sites, and the script used for the formulation STEEP model presented in this study can be accessed
633 at <https://doi.org/10.5281/zenodo.7109044>. H data for the SET site is publicly available for download
634 at <https://ameriflux.lbl.gov/>.

635 **References**

636 Akoglu, H. (2018). User's guide to correlation coefficients. Turkish journal of emergency medicine,
637 18(3), 91-93. doi: 10.1016/j.tjem.2018.08.001

638 Alberton, B., Torres, R. da S., Cancian, L. F., Borges, B. D., Almeida, J., Mariano, G. C., ... Morellato,
639 L. P. C. (2017). Introducing digital cameras to monitor plant phenology in the tropics: applications for
640 conservation. *Perspectives in Ecology and Conservation*, 15(2), 82–90.
641 doi:10.1016/j.pecon.2017.06.004

642 Allam, M., Mhaweij, M., Meng, Q., Faour, G., Abunnasr, Y., Fadel, A., & Xinli, H. (2021). Monthly 10-
643 m evapotranspiration rates retrieved by SEBALI with Sentinel-2 and MODIS LST data. *Agricultural*
644 *Water Management*, 243, 106432. doi:10.1016/j.agwat.2020.106432

645 Allen, R. G., Tasumi, M., & Trezza, R. (2007). Satellite-Based Energy Balance for Mapping
646 Evapotranspiration with Internalized Calibration (METRIC)—Model. *Journal of Irrigation and*
647 *Drainage Engineering*, 133(4), 380–394. doi:10.1061/(asce)0733-9437(2007)133:4(380)

648 Allen, K., Dupuy, J. M., Gei, M. G., Hulshof, C., Medvigy, D., Pizano, C., ... Powers, J. S. (2017).
649 Will seasonally dry tropical forests be sensitive or resistant to future changes in rainfall regimes?
650 *Environmental Research Letters*, 12(2), 023001. doi:10.1088/1748-9326/aa5968

651 Allen, R. G., Pereira, L. S., Howell, T. A., & Jensen, M. E. (2011). Evapotranspiration information
652 reporting: I. Factors governing measurement accuracy. *Agricultural Water Management*, 98(6), 899–
653 920. doi:10.1016/j.agwat.2010.12.015

654 Alvares, C. A., Stape, J. L., Sentelhas, P. C., Gonçalves, J. D. M., & Sparovek, G. (2013). Köppen's
655 climate classification map for Brazil. *Meteorologische Zeitschrift*, 22(6), 711-728. doi:10.1127/0941-
656 2948/2013/0507

657 Anapalli, S. S., Ahuja, L. R., Gowda, P. H., Ma, L., Marek, G., Evett, S. R., & Howell, T. A. (2016).
658 Simulation of crop evapotranspiration and crop coefficients with data in weighing lysimeters.
659 *Agricultural Water Management*, 177, 274–283. doi:10.1016/j.agwat.2016.08.009

660 Andrade, J., Cunha, J., Silva, J., Rufino, I., & Galvão, C. (2021). Evaluating single and multi-date
661 Landsat classifications of land-cover in a seasonally dry tropical forest. *Remote Sensing*
662 *Applications: Society and Environment*, 22, 100515. doi:10.1016/j.rsase.2021.100515

663 Anderson, M. C., Kustas, W. P., Norman, J. M., Hain, C. R., Mecikalski, J. R., Schultz, L., ... Gao,
664 F. (2011). Mapping daily evapotranspiration at field to continental scales using geostationary and
665 polar orbiting satellite imagery. *Hydrology and Earth System Sciences*, 15(1), 223–239.
666 doi:10.5194/hess-15-223-2011

667 Antonino, A. C. D. (2019), AmeriFlux BASE BR-CST Caatinga Serra Talhada, Ver. 1-5, AmeriFlux
668 AMP, (Dataset). <https://doi.org/10.17190/AMF/1562386>

669 Araújo, J. C., & González Piedra, J. I. (2009). Comparative hydrology: analysis of a semiarid and a
670 humid tropical watershed. *Hydrological Processes*, 23(8), 1169–1178. doi:10.1002/hyp.7232

671 Barbosa, H. A., Huete, A. R., & Baethgen, W. E. (2006). A 20-year study of NDVI variability over the
672 Northeast Region of Brazil. *Journal of Arid Environments*, 67(2), 288–307.
673 doi:10.1016/j.jaridenv.2006.02.022

674 Barraza, V., Restrepo-Coupe, N., Huete, A., Grings, F., Beringer, J., Cleverly, J., & Eamus, D.
675 (2017). Estimation of latent heat flux over savannah vegetation across the North Australian Tropical
676 Transect from multiple sensors and global meteorological data. *Agricultural and Forest Meteorology*,
677 232, 689-703. doi:10.1016/j.agrformet.2016.10.013

678 Bastiaanssen, W. G. M. (1995). Regionalization of surface flux densities and moisture indicators in
679 composite terrain: A remote sensing approach under clear skies in Mediterranean climates.
680 Wageningen University and Research.

681 Bastiaanssen, W. G. M., Menenti, M., Feddes, R. A., & Holtslag, A. A. M. (1998). A remote sensing
682 surface energy balance algorithm for land (SEBAL). 1. Formulation. *Journal of Hydrology*, 212-213,
683 198–212. doi:10.1016/s0022-1694(98)00253-4

684 Bastiaanssen, W. G. M., Ahmad, M.-D., & Chemin, Y. (2002). Satellite surveillance of evaporative
685 depletion across the Indus Basin. *Water Resources Research*, 38(12), 9–1–9–9.
686 doi:10.1029/2001wr000386

687 Bastiaanssen, W. G. M., Noordman, E. J. M., Pelgrum, H., Davids, G., Thoreson, B. P., & Allen, R.
688 G. (2005). SEBAL Model with Remotely Sensed Data to Improve Water-Resources Management
689 under Actual Field Conditions. *Journal of Irrigation and Drainage Engineering*, 131(1), 85–93.
690 doi:10.1061/(asce)0733-9437(2005)131:1(85)

691 Beven, K., & Freer, J. (2001). Equifinality, data assimilation, and uncertainty estimation in
692 mechanistic modelling of complex environmental systems using the GLUE methodology. *Journal of*
693 *Hydrology*, 249(1–4), 11–29. doi:10.1016/s0022-1694(01)00421-8

694 Bhattarai, N., Quackenbush, L. J., Im, J., & Shaw, S. B. (2017). A new optimized algorithm for
695 automating endmember pixel selection in the SEBAL and METRIC models. *Remote Sensing of*
696 *Environment*, 196, 178–192. doi:10.1016/j.rse.2017.05.009.

697 Biggs, T. W., Marshall, M., & Messina, A. (2016). Mapping daily and seasonal evapotranspiration
698 from irrigated crops using global climate grids and satellite imagery: Automation and methods
699 comparison. *Water Resources Research*, 52(9), 7311–7326. doi:10.1002/2016wr019107

700 Borges, C. K., dos Santos, C. A. C., Carneiro, R. G., da Silva, L. L., de Oliveira, G., Mariano, D., ...
701 de S. Medeiros, S. (2020). Seasonal variation of surface radiation and energy balances over two
702 contrasting areas of the seasonally dry tropical forest (Caatinga) in the Brazilian semi-arid.
703 *Environmental Monitoring and Assessment*, 192(8). doi:10.1007/s10661-020-08484-y

704 Brazil, Ministério do Meio Ambiente. Caatinga. <https://antigo.mma.gov.br/biomas/caatinga.html>.
705 Accessed date: 25 March 2021.

706 Cabral, O. M. R., Freitas, H. C., Cuadra, S. V., de Andrade, C. A., Ramos, N. P., Grutzmacher, P.,
707 ... Rossi, P. (2020). The sustainability of a sugarcane plantation in Brazil assessed by the eddy
708 covariance fluxes of greenhouse gases. *Agricultural and Forest Meteorology*, 282-283, 107864.
709 doi:10.1016/j.agrformet.2019.107864

710 Campos, S., Mendes, K. R., da Silva, L. L., Mutti, P. R., Medeiros, S. S., Amorim, L. B., ... Bezerra,
711 B. G. (2019). Closure and partitioning of the energy balance in a preserved area of a Brazilian

712 seasonally dry tropical forest. *Agricultural and Forest Meteorology*, 271, 398–412.
713 doi:10.1016/j.agrformet.2019.03.018

714 Carvalho, H. F. D. S., de Moura, M. S., da Silva, T. G., & Rodrigues, C. T. (2018). Controlling factors
715 of 'Caatinga' and sugarcane evapotranspiration in the Sub-middle São Francisco Valley. *Revista*
716 *Brasileira de Engenharia Agrícola e Ambiental*, 22, 225-230. doi:10.1590/1807-
717 1929/agriambi.v22n4p225-230

718 Chai, T., & Draxler, R. R. (2014). Root mean square error (*RMSE*) or mean absolute error (*MAE*)?
719 – Arguments against avoiding *RMSE* in the literature. *Geoscientific Model Development*, 7(3), 1247–
720 1250. doi:10.5194/gmd-7-1247-2014

721 Chehbouni, A., Seen, D. L., Njoku, E. G., & Monteny, B. M. (1996). Examination of the difference
722 between radiative and aerodynamic surface temperatures over sparsely vegetated surfaces. *Remote*
723 *Sensing of Environment*, 58(2), 177-186. doi: 10.1016/S0034-4257(96)00037-5

724 Chen, J. M., & Liu, J. (2020). Evolution of evapotranspiration models using thermal and shortwave
725 remote sensing data. *Remote Sensing of Environment*, 237, 111594. doi:10.1016/j.rse.2019.111594

726 Chen, H., Gnanamoorthy, P., Chen, Y., Mansaray, L. R., Song, Q., Liao, K., ... Sun, C. (2022).
727 Assessment and Inter-Comparison of Multi-Source High Spatial Resolution Evapotranspiration
728 Products over Lancang–Mekong River Basin, Southeast Asia. *Remote Sensing*, 14(3), 479.
729 doi:10.3390/rs14030479

730 Cheng, M., Jiao, X., Li, B., Yu, X., Shao, M., & Jin, X. (2021). Long time series of daily
731 evapotranspiration in China based on the SEBAL model and multisource images and validation.
732 *Earth System Science Data*, 13(8), 3995–4017. doi:10.5194/essd-13-3995-2021

733 Costa, J. A.; Navarro-Hevia, J., Costa, C. A. G., & de Araújo, J. C. (2021). Temporal dynamics of
734 evapotranspiration in semiarid native forests in Brazil and Spain using remote sensing. *Hydrological*
735 *Processes*, 35(3). doi:10.1002/hyp.14070

736 Costa-Filho, E., Chávez, J. L., Zhang, H., & Andales, A. A. (2021). An optimized surface aerodynamic
737 temperature approach to estimate maize sensible heat flux and evapotranspiration. *Agricultural and*
738 *Forest Meteorology*, 311, 108683. doi:10.1016/j.agrformet.2021.108683

739 Cunha, J., Nóbrega, R. L. B., Rufino, I., Erasmi, S., Galvão, C., & Valente, F. (2020). Surface albedo
740 as a proxy for land-cover clearing in seasonally dry forests: Evidence from the Brazilian Caatinga.
741 *Remote Sensing of Environment*, 238, 111250. doi:10.1016/j.rse.2019.111250

742 Danelichen, V. H. de M., Biudes, M. S., Souza, M. C., Machado, N. G., Silva, B. B. da, & Nogueira,
743 J. de S. (2014). Estimation of soil heat flux in a neotropical Wetland region using remote sensing
744 techniques. *Revista Brasileira de Meteorologia*, 29(4), 469–482. doi:10.1590/0102-778620120568

745 Dombroski, J. L. D., Praxedes, S. C., de Freitas, R. M. O., & Pontes, F. M. (2011). Water relations
746 of Caatinga trees in the dry season. *South African Journal of Botany*, 77(2), 430–434.
747 doi:10.1016/j.sajb.2010.11.001

748 Farr, T. G., Rosen, P. A., Caro, E., Crippen, R., Duren, R., Hensley, S., ... & Alsdorf, D. (2007). The
749 shuttle radar topography mission. *Reviews of geophysics*, 45(2). doi:10.1029/2005RG000183

750 Ferreira, T. R., Silva, B. B. D., Moura, M. S. B. D., Verhoef, A., & Nóbrega, R. L. B. (2020). The use
751 of remote sensing for reliable estimation of net radiation and its components: a case study for
752 contrasting land covers in an agricultural hotspot of the Brazilian semiarid region. *Agricultural and*
753 *Forest Meteorology*, 291, 108052. doi:10.1016/j.agrformet.2020.108052

754 Foken, T. (2008). The energy balance closure problem: An overview. *Ecological Applications*, 18(6),
755 1351-1367. doi:10.1890/06-0922.1

756 French, A. N., Hunsaker, D. J., & Thorp, K. R. (2015). Remote sensing of evapotranspiration over
757 cotton using the TSEB and METRIC energy balance models. *Remote Sensing of Environment*, 158,
758 281–294. doi:10.1016/j.rse.2014.11.003

759 Funk, C., Peterson, P., Landsfeld, M., Pedreros, D., Verdin, J., Shukla, S., ... & Michaelsen, J. (2015).
760 The climate hazards infrared precipitation with stations—a new environmental record for monitoring
761 extremes. *Scientific data*, 2(1), 1-21. doi:10.1038/sdata.2015.66

762 Gan, R., Zhang, Y., Shi, H., Yang, Y., Eamus, D., Cheng, L., ... Yu, Q. (2018). Use of satellite leaf
763 area index estimating evapotranspiration and gross assimilation for Australian ecosystems.
764 *Ecohydrology*, 11(5), e1974. doi:10.1002/eco.1974

765 Gokmen, M., Vekerdy, Z., Verhoef, A., Verhoef, W., Batelaan, O., & van der Tol, C. (2012).
766 Integration of soil moisture in SEBS for improving evapotranspiration estimation under water stress
767 conditions. *Remote Sensing of Environment*, 121, 261–274. doi:10.1016/j.rse.2012.02.003

768 Gorelick, N., Hancher, M., Dixon, M., Ilyushchenko, S., Thau, D., & Moore, R. (2017). Google Earth
769 Engine: Planetary-scale geospatial analysis for everyone. *Remote Sensing of Environment*, 202,
770 18–27. doi:10.1016/j.rse.2017.06.031

771 Gupta, H. V., Sorooshian, S., & Yapo, P. O. (1999). Status of automatic calibration for hydrologic
772 models: Comparison with multilevel expert calibration. *Journal of hydrologic engineering*, 4(2), 135-
773 143. doi:10.1061/(ASCE)1084-0699(1999)4:2(135)

774 Hallak, R., & Pereira Filho, A. J. (2011). Metodologia para análise de desempenho de simulações
775 de sistemas convectivos na região metropolitana de São Paulo com o modelo ARPS: sensibilidade
776 a variações com os esquemas de advecção e assimilação de dados. *Revista Brasileira de*
777 *Meteorologia*, 26, 591-608. doi:10.1590/S0102-77862011000400009

778 Hollinger, D. Y., & Richardson, A. D. (2005). Uncertainty in eddy covariance measurements and its
779 application to physiological models. *Tree Physiology*, 25(7), 873–885.
780 doi:10.1093/treephys/25.7.873

781 Jaafar, H., Mourad, R., & Schull, M. (2022). A global 30-m ET model (HSEB) using harmonized
782 Landsat and Sentinel-2, MODIS and VIIRS: Comparison to ECOSTRESS ET and LST. *Remote*
783 *Sensing of Environment*, 274, 112995. doi:10.1016/j.rse.2022.112995

784 Jia, L., Su, Z., van den Hurk, B., Menenti, M., Moene, A., De Bruin, H. A. ., ... Cuesta, A. (2003).
785 Estimation of sensible heat flux using the Surface Energy Balance System (SEBS) and ATSR
786 measurements. *Physics and Chemistry of the Earth, Parts A/B/C*, 28(1-3), 75–88.
787 doi:10.1016/s1474-7065(03)00009-3

788 Kayser, R. H., Ruhoff, A., Laipelt, L., de Mello Kich, E., Roberti, D. R., de Arruda Souza, V., ... &
789 Neale, C. M. U. (2022). Assessing geeSEBAL automated calibration and meteorological reanalysis
790 uncertainties to estimate evapotranspiration in subtropical humid climates. *Agricultural and Forest*
791 *Meteorology*, 314, 108775. doi:10.1016/j.agrformet.2021.108775

792 Koch, R., Almeida-Cortez, J. S., & Kleinschmit, B. (2017). Revealing areas of high nature
793 conservation importance in a seasonally dry tropical forest in Brazil: Combination of modelled plant
794 diversity hot spots and threat patterns. *Journal for Nature Conservation*, 35, 24–39.
795 doi:10.1016/j.jnc.2016.11.004

796 Kustas, W., Choudhury, B. Moran, M. Reginato, R. ., Jackson, R. ., Gay, L. ., & Weaver, H. . (1989).
797 Determination of sensible heat flux over sparse canopy using thermal infrared data. *Agricultural and*
798 *Forest Meteorology*, 44(3-4), 197–216. doi:10.1016/0168-1923(89)90017-8

799 Kustas, W. P., Choudhury, B. J., Kunkel, K. E., & Gay, L. W. (1989). Estimate of the aerodynamic
800 roughness parameters over an incomplete canopy cover of cotton. *Agricultural and Forest*
801 *Meteorology*, 46(1-2), 91-105. doi:10.1016/0168-1923(89)90114-7

802 Laipelt, L., Ruhoff, A. L., Fleischmann, A. S., Kayser, R. H. B., Kich, E. de M., da Rocha, H. R., &
803 Neale, C. M. U. (2020). Assessment of an Automated Calibration of the SEBAL Algorithm to Estimate
804 Dry-Season Surface-Energy Partitioning in a Forest–Savanna Transition in Brazil. *Remote Sensing*,
805 12(7), 1108. doi:10.3390/rs12071108

806 Laipelt, L., Henrique Bloedow Kayser, R., Santos Fleischmann, A., Ruhoff, A., Bastiaanssen, W.,
807 Erickson, T. A., & Melton, F. (2021). Long-term monitoring of evapotranspiration using the SEBAL
808 algorithm and Google Earth Engine cloud computing. *ISPRS Journal of Photogrammetry and*
809 *Remote Sensing*, 178, 81–96. doi:10.1016/j.isprsjprs.2021.05.018

810 Lhomme, J. P., Chehbouni, A., & Monteny, B. (2000). Sensible Heat Flux-Radiometric Surface
811 Temperature Relationship Over Sparse Vegetation: Parameterizing B-1. *Boundary-Layer
812 Meteorology*, 97(3), 431–457. doi:10.1023/a:1002786402695

813 Lima, A. L. A., & Rodal, M. J. N. (2010). Phenology and wood density of plants growing in the semi-
814 arid region of northeastern Brazil. *Journal of Arid Environments*, 74(11), 1363–1373.
815 doi:10.1016/j.jaridenv.2010.05.009

816 Lima, A. L. A., Sá Barretto Sampaio, E. V., Castro, C. C., Rodal, M. J. N., Antonino, A. C. D., & de
817 Melo, A. L. (2012). Do the phenology and functional stem attributes of woody species allow for the
818 identification of functional groups in the semiarid region of Brazil? *Trees*, 26(5), 1605–1616.
819 doi:10.1007/s00468-012-0735-2

820 Lima, C. E. S. de, Costa, V. S. de O., Galvíncio, J. D., Silva, R. M. da, & Santos, C. A. G. (2021).
821 Assessment of automated evapotranspiration estimates obtained using the GP-SEBAL algorithm for
822 dry forest vegetation (Caatinga) and agricultural areas in the Brazilian semiarid region. *Agricultural
823 Water Management*, 250, 106863. doi:10.1016/j.agwat.2021.106863

824 Liao, J. J., & Lewis, J. W. (2000). A note on concordance correlation coefficient. *PDA journal of
825 pharmaceutical science and technology*, 54(1), 23-26.

826 Lin, L. K. (1989). A Concordance Correlation Coefficient to Evaluate Reproducibility. *Biometrics*,
827 45(1), 255–268. <https://doi.org/10.2307/2532051>

828 Liu, S., Lu, L., Mao, D., & Jia, L. (2007). Evaluating parameterizations of aerodynamic resistance to
829 heat transfer using field measurements. *Hydrology and Earth System Sciences*, 11(2), 769–783.
830 doi:10.5194/hess-11-769-2007

831 Liu, Y., Guo, W., Huang, H., Ge, J., & Qiu, B. (2021). Estimating global aerodynamic parameters in
832 1982–2017 using remote-sensing data and a turbulent transfer model. *Remote Sensing of
833 Environment*, 260, 112428. doi:10.1016/j.rse.2021.112428

834 Long, D., Gao, Y., & Singh, V. P. (2010). Estimation of daily average net radiation from MODIS data
835 and DEM over the Baiyangdian watershed in North China for clear sky days. *Journal of Hydrology*,
836 388(3–4), 217–233. doi:10.1016/j.jhydrol.2010.04.042

837 Maia, V. A., de Souza, C. R., de Aguiar-Campos, N., Fagundes, N. C. A., Santos, A. B. M., de Paula,
838 G. G. P., ... dos Santos, R. M. (2020). Interactions between climate and soil shape tree community
839 assembly and above-ground woody biomass of tropical dry forests. *Forest Ecology and*
840 *Management*, 474, 118348. doi:10.1016/j.foreco.2020.118348

841 Marques, T. V., Mendes, K., Mutti, P., Medeiros, S., Silva, L., Perez-Marin, A. M., ... Bezerra, B.
842 (2020). Environmental and biophysical controls of evapotranspiration from Seasonally Dry Tropical
843 Forests (Caatinga) in the Brazilian Semiarid. *Agricultural and Forest Meteorology*, 287, 107957.
844 doi:10.1016/j.agrformet.2020.107957

845 McShane, R. R., Driscoll, K. P., & Sando, R. (2017). A review of surface energy balance models for
846 estimating actual evapotranspiration with remote sensing at high spatiotemporal resolution over
847 large extents. *Scientific Investigations Report*. doi:10.3133/sir20175087

848 Medeiros, R., Andrade, J., Ramos, D., Moura, M., Pérez-Marin, A., dos Santos, C., ... Cunha, J.
849 (2022). Remote Sensing Phenology of the Brazilian Caatinga and Its Environmental Drivers. *Remote*
850 *Sensing*, 14(11), 2637. doi:10.3390/rs14112637

851 Melo, D. C. D., Anache, J. A. A., Borges, V. P., Miralles, D. G., Martens, B., Fisher, J. B., ...
852 Wendland, E. (2021). Are Remote Sensing Evapotranspiration Models Reliable Across South
853 American Ecoregions? *Water Resources Research*, 57(11). doi:10.1029/2020wr028752

854 Mhaweji, M., Caiserman, A., Nasrallah, A., Dawi, A., Bachour, R., & Faour, G. (2020). Automated
855 evapotranspiration retrieval model with missing soil-related datasets: The proposal of SEBALL.
856 *Agricultural Water Management*, 229, 105938. doi:10.1016/j.agwat.2019.105938

857 Miles, L., Newton, A. C., DeFries, R. S., Ravillious, C., May, I., Blyth, S., ... Gordon, J. E. (2006). A
858 global overview of the conservation status of tropical dry forests. *Journal of Biogeography*, 33(3),
859 491–505. doi:10.1111/j.1365-2699.2005.01424.x

860 Miranda, R. Q., Nóbrega, R. L. B., Moura, M. S. B., Raghavan, S., & Galvêncio, J. D. (2020). Realistic
861 and simplified models of plant and leaf area indices for a seasonally dry tropical forest. *International*
862 *Journal of Applied Earth Observation and Geoinformation*, 85, 101992.
863 doi:10.1016/j.jag.2019.101992

864 Miranda, R. D. Q., Galvencio, J. D., Morais, Y. C. B., MOURA, M. S. B. D., Jones, C. A., & Srinivasan,
865 R. (2018). Dry forest deforestation dynamics in Brazil's Pontal Basin. *Revista Caatinga*, 31, 385-395.
866 doi:10.1590/1983-21252018v31n215rc

867 Mohan, M. M. P., Kanchirapuzha, R., & Varma, M. R. R. (2020a). Review of approaches for the
868 estimation of sensible heat flux in remote sensing-based evapotranspiration models. *Journal of*
869 *Applied Remote Sensing*, 14(04). doi:10.1117/1.jrs.14.041501

870 Mohan, M. P.; Kanchirapuzha, R., & Varma, M. R. R. (2020b). Integration of soil moisture as an
871 auxiliary parameter for the anchor pixel selection process in SEBAL using Landsat 8 and Sentinel-
872 1A images. *International Journal of Remote Sensing*, 41(3), 1214-1231.

873 Moro, M. F., Silva, I. A., Araújo, F. S. de, Nic Lughadha, E., Meagher, T. R., & Martins, F. R. (2015).
874 The Role of Edaphic Environment and Climate in Structuring Phylogenetic Pattern in Seasonally Dry
875 Tropical Plant Communities. *PLOS ONE*, 10(3), e0119166. doi:10.1371/journal.pone.0119166

876 Moro, M. F., Nic Lughadha, E., de Araújo, F. S., & Martins, F. R. (2016). A Phytogeographical
877 Metaanalysis of the Semiarid Caatinga Domain in Brazil. *The Botanical Review*, 82(2), 91–148.
878 doi:10.1007/s12229-016-9164-z

879 Mu, Q., Zhao, M., & Running, S. W. (2011). Improvements to a MODIS global terrestrial
880 evapotranspiration algorithm. *Remote Sensing of Environment*, 115(8), 1781–1800.
881 doi:10.1016/j.rse.2011.02.019

882 Muñoz Sabater, J., (2019): ERA5-Land hourly data from 1981 to present. Copernicus Climate
883 Change Service (C3S) Climate Data Store (CDS). (Accessed on 23-Feb-2022),
884 doi:10.24381/cds.e2161bac

885 Mutti, P. R., da Silva, L. L., Medeiros, S. de S., Dubreuil, V., Mendes, K. R., Marques, T. V., ...
886 Bezerra, B. G. (2019). Basin scale rainfall-evapotranspiration dynamics in a tropical semiarid
887 environment during dry and wet years. *International Journal of Applied Earth Observation and*
888 *Geoinformation*, 75, 29–43. doi:10.1016/j.jag.2018.10.007

889 Murray, T., and Verhoef, A. (2007) Moving towards a more mechanistic approach in the
890 determination of soil heat flux from remote measurements. II. Diurnal shape of soil heat flux.
891 *Agricultural and Forest Meteorology*, 147: 88-97.

892 Nash, J. E., & Sutcliffe, J. V. (1970). River flow forecasting through conceptual models part I - A
893 discussion of principles. *Journal of Hydrology*, 10(3), 282–290. doi:10.1016/0022-1694(70)90255-6

894 Oliveira, M. L., Santos, C. A. C., Oliveira, G., Perez-Marin, A. M., & Santos, C. A. G. (2021). Effects
895 of human-induced land degradation on water and carbon fluxes in two different Brazilian dryland soil
896 covers. *Science of The Total Environment*, 792, 148458. doi:10.1016/j.scitotenv.2021.148458

897 Owen, P. R., & Thomson, W. R. (1963). Heat transfer across rough surfaces. *Journal of Fluid*
898 *Mechanics*, 15(3), 321–334. doi:10.1017/s0022112063000288

899 Paloschi, R. A., Ramos, D. M., Ventura, D. J., Souza, R., Souza, E., Morellato, L. P. C., ... Borma,
900 L. D. S. (2020). Environmental Drivers of Water Use for Caatinga Woody Plant Species: Combining
901 Remote Sensing Phenology and Sap Flow Measurements. *Remote Sensing*, 13(1), 75.
902 doi:10.3390/rs13010075

903 Paul, G., Gowda, P. H., Vara Prasad, P. V., Howell, T. A., Staggenborg, S. A., & Neale, C. M. U.
904 (2013). Lysimetric evaluation of SEBAL using high resolution airborne imagery from BEAREX08.
905 *Advances in Water Resources*, 59, 157–168. doi:10.1016/j.advwatres.2013.06.003

906 Paul, G., Gowda, P. H., Vara Prasad, P. V., Howell, T. A., Aiken, R. M., & Neale, C. M. U. (2014).
907 Investigating the influence of roughness length for heat transport (zoh) on the performance of SEBAL
908 in semi-arid irrigated and dryland agricultural systems. *Journal of Hydrology*, 509, 231–244.
909 doi:10.1016/j.jhydrol.2013.11.040

910 Paulson, C. A. (1970). The mathematical representation of wind speed and temperature profiles in
911 the unstable atmospheric surface layer. *Journal of Applied Meteorology and Climatology*, 9(6), 857-
912 861. doi:10.1175/1520-0450(1970)009%3C0857:tmrows%3E2.0.co;2

913 Pennington, R. T., Lewis, G. P., & Ratter, J. A. (Eds.). (2006). An Overview of the Plant Diversity,
914 Biogeography and Conservation of Neotropical Savannas and Seasonally Dry Forests. *Neotropical*
915 *Savannas and Seasonally Dry Forests*, 1–29. doi:10.1201/9781420004496-1

916 Pennington, R. T., Lavin, M., & Oliveira-Filho, A. (2009). Woody Plant Diversity, Evolution, and
917 Ecology in the Tropics: Perspectives from Seasonally Dry Tropical Forests. *Annual Review of*
918 *Ecology, Evolution, and Systematics*, 40(1), 437–457. doi:10.1146/annurev.ecolsys.110308.120327

919 Pennington, R. T., Lehmann, C. E. R., & Rowland, L. M. (2018). Tropical savannas and dry forests.
920 *Current Biology*, 28(9), R541–R545. doi:10.1016/j.cub.2018.03.014

921 Potapov, P., Li, X., Hernandez-Serna, A., Tyukavina, A., Hansen, M. C., Kommareddy, A., ... Hofton,
922 M. (2021). Mapping global forest canopy height through integration of GEDI and Landsat data.
923 *Remote Sensing of Environment*, 253, 112165. doi:10.1016/j.rse.2020.112165

924 Priestley, C. H. B., & Taylor, R. J. (1972). On the Assessment of Surface Heat Flux and Evaporation
925 Using Large-Scale Parameters. *Monthly Weather Review*, 100(2), 81–92. doi:10.1175/1520-
926 0493(1972)100<0081:otaosh>2.3.co;2

927 Queiroz, L. P., Cardoso, D., Fernandes, M. F., & Moro, M. F. (2017). Diversity and Evolution of
928 Flowering Plants of the Caatinga Domain. *Caatinga*, 23–63. doi:10.1007/978-3-319-68339-3_2

929 Queiroz, M. G. D., Silva, T. G. F. D., Souza, C. A. A. D., Jardim, A. M. D. R. F., Araújo Júnior, G. D.
930 N., Souza, L. S. B. D., & Moura, M. S. B. D. (2020). Composition of Caatinga species under anthropic

931 disturbance and its correlation with rainfall partitioning. *Floresta e Ambiente*, 28. doi:10.1590/2179-
932 8087-FLORAM-2019-0044

933 Ramoelo, A., Majozi, N., Mathieu, R., Jovanovic, N., Nickless, A., & Dzikiti, S. (2014). Validation of
934 Global Evapotranspiration Product (MOD16) using Flux Tower Data in the African Savanna, South
935 Africa. *Remote Sensing*, 6(8), 7406–7423. doi:10.3390/rs6087406

936 Rasp, S., Pritchard, M. S., & Gentine, P. (2018). Deep learning to represent subgrid processes in
937 climate models. *Proceedings of the National Academy of Sciences*, 115(39), 9684–9689.
938 doi:10.1073/pnas.1810286115

939 Roberts, W., Williams, G. P., Jackson, E., Nelson, E. J., & Ames, D. P. (2018). Hydrostats: A Python
940 Package for Characterizing Errors between Observed and Predicted Time Series. *Hydrology*, 5(4),
941 66. doi:10.3390/hydrology5040066

942 Rodell, M., Houser, P. R., Jambor, U., Gottschalck, J., Mitchell, K., Meng, C.-J., ... Toll, D. (2004).
943 The Global Land Data Assimilation System. *Bulletin of the American Meteorological Society*, 85(3),
944 381–394. doi:10.1175/bams-85-3-381

945 Running, S., Mu, Q., Zhao, M. (2017). MOD16A2 MODIS/Terra Net Evapotranspiration 8-Day L4
946 Global 500m SIN Grid V006 [Data set]. NASA EOSDIS Land Processes DAAC. Accessed 23-Feb-
947 2022 from doi:10.5067/MODIS/MOD16A2.006

948 Sahnoun, F., Abderrahmane, H., Kaddour, M., Abdelkader, K., Mohamed, B., & Castro, T. A. H. D.
949 (2021). Application of SEBAL and T s/VI Trapezoid Models for Estimating Actual Evapotranspiration
950 in the Algerian Semi-Arid Environment to Improve Agricultural Water Management. *Revista*
951 *Brasileira de Meteorologia*, 36, 219-236. doi:10.1590/0102-77863610020

952 Salazar-Martínez, D., Holwerda, F., Holmes, T. R. H., Yépez, E. A., Hain, C. R., Alvarado-Barrientos,
953 S., ... Vivoni, E. R. (2022). Evaluation of remote sensing-based evapotranspiration products at low-
954 latitude eddy covariance sites. *Journal of Hydrology*, 610, 127786.
955 doi:10.1016/j.jhydrol.2022.127786

956 Santos, R. M., Oliveira-Filho, A. T., Eisenlohr, P. V., Queiroz, L. P., Cardoso, D. B. O. S., & Rodal,
957 M. J. N. (2012). Identity and relationships of the Arboreal Caatinga among other floristic units of
958 seasonally dry tropical forests (SDTFs) of north-eastern and Central Brazil. *Ecology and Evolution*,
959 2(2), 409–428. doi:10.1002/ece3.91

960 Santos, M. G., Oliveira, M. T., Figueiredo, K. V., Falcão, H. M., Arruda, E. C. P., Almeida-Cortez, J.,
961 ... Antonino, A. C. D. (2014). Caatinga, the Brazilian dry tropical forest: can it tolerate climate
962 changes? *Theoretical and Experimental Plant Physiology*, 26(1), 83–99. doi:10.1007/s40626-014-
963 0008-0

964 Santos, C. A. C., Mariano, D. A., das Chagas A. do Nascimento, F., da C. Dantas, F. R., de Oliveira,
965 G., Silva, M. T., ... Neale, C. M. U. (2020). Spatio-temporal patterns of energy exchange and
966 evapotranspiration during an intense drought for drylands in Brazil. *International Journal of Applied*
967 *Earth Observation and Geoinformation*, 85, 101982. doi:10.1016/j.jag.2019.101982

968 Schaaf, C., & Wang, Z. (2015). MCD43A4 MODIS/Terra+Aqua BRDF/Albedo Nadir BRDF Adjusted
969 Ref Daily L3 Global - 500m V006 [Data set]. NASA EOSDIS Land Processes DAAC. Accessed 23-
970 Feb-2022 from doi:10.5067/MODIS/MCD43A4.006

971 Senay, G. B., Bohms, S., Singh, R. K., Gowda, P. H., Velpuri, N. M., Alemu, H., & Verdin, J. P.
972 (2013). Operational Evapotranspiration Mapping Using Remote Sensing and Weather Datasets: A
973 New Parameterization for the SSEB Approach. *JAWRA Journal of the American Water Resources*
974 *Association*, 49(3), 577–591. Portico. <https://doi.org/10.1111/jawr.12057>

975 Senay, G. B., Friedrichs, M., Morton, C., Parrish, G. E., Schauer, M., Khand, K., ... & Huntington, J.
976 (2022). Mapping actual evapotranspiration using Landsat for the conterminous United States:
977 Google Earth Engine implementation and assessment of the SSEBop model. *Remote Sensing of*
978 *Environment*, 275, 113011. doi:10.1016/j.rse.2022.113011

979 Senkondo, W., Munishi, S. E., Tumbo, M., Nobert, J., & Lyon, S. W. (2019). Comparing Remotely-
980 Sensed Surface Energy Balance Evapotranspiration Estimates in Heterogeneous and Data-Limited

- 981 Regions: A Case Study of Tanzania's Kilombero Valley. *Remote Sensing*, 11(11), 1289.
982 doi:10.3390/rs11111289
- 983 Shuttleworth, W. J. (2012). *Terrestrial hydrometeorology*. John Wiley & Sons.
- 984 Silva, A. M., da Silva, R. M., & Santos, C. A. G. (2019). Automated surface energy balance algorithm
985 for land (ASEBAL) based on automating endmember pixel selection for evapotranspiration
986 calculation in MODIS orbital images. *International Journal of Applied Earth Observation and*
987 *Geoinformation*, 79, 1–11. doi:10.1016/j.jag.2019.02.012
- 988 Silva, J. M. C.; LEAL, I.R.; TABARELLI, M. (Ed.). (2017a). *Caatinga: the largest tropical dry forest*
989 *region in South America*. Springer.
- 990 Silva, P. F. da, Lima, J. R. de S., Antonino, A. C. D., Souza, R., Souza, E. S. de, Silva, J. R. I., &
991 Alves, E. M. (2017b). Seasonal patterns of carbon dioxide, water and energy fluxes over the
992 Caatinga and grassland in the semi-arid region of Brazil. *Journal of Arid Environments*, 147, 71–82.
993 doi:10.1016/j.jaridenv.2017.09.003
- 994 Singh, R. K., & Irmak, A. (2011). Treatment of anchor pixels in the METRIC model for improved
995 estimation of sensible and latent heat fluxes. *Hydrological Sciences Journal*, 56(5), 895–906.
996 doi:10.1080/02626667.2011.587424
- 997 Singh, R. K., Liu, S., Tieszen, L. L., Suyker, A. E., & Verma, S. B. (2012). Estimating seasonal
998 evapotranspiration from temporal satellite images. *Irrigation Science*, 30(4), 303-313.
999 doi:10.1007/s00271-011-0287-z
- 1000 Souza, L. S. B. de, Moura, M. S. B. de, Sedyama, G. C., & Silva, T. G. F. da. (2015). Balanço de
1001 energia e controle biofísico da evapotranspiração na Caatinga em condições de seca intensa.
1002 *Pesquisa Agropecuária Brasileira*, 50(8), 627–636. doi:10.1590/s0100-204x2015000800001
- 1003 Stewart, J. B., Kustas, W. P., Humes, K. S., Nichols, W. D., Moran, M. S., & de Bruin, H. A. (1994).
1004 Sensible heat flux-radiometric surface temperature relationship for eight semiarid areas. *Journal of*

1005 Applied Meteorology and Climatology, 33(9), 1110-1117. doi:10.1175/1520-
1006 0450(1994)033%3C1110:shfrst%3E2.0.co;2

1007 Su, Z., Schmugge, T., Kustas, W. P., & Massman, W. J. (2001). An evaluation of two models for
1008 estimation of the roughness height for heat transfer between the land surface and the atmosphere.
1009 Journal of applied meteorology, 40(11), 1933-1951. doi:10.1175/1520-
1010 0450(2001)040%3C1933:aeotmf%3E2.0.co;2

1011 Su, Z. (2002). The Surface Energy Balance System (SEBS) for estimation of turbulent heat fluxes.
1012 Hydrology and Earth System Sciences, 6(1), 85–100. doi:10.5194/hess-6-85-2002

1013 Teixeira, A. D. C., Bastiaanssen, W. G., Ahmad, M., & Bos, M. G. (2009). Reviewing SEBAL input
1014 parameters for assessing evapotranspiration and water productivity for the Low-Middle Sao
1015 Francisco River basin, Brazil: Part A: Calibration and validation. Agricultural and forest meteorology,
1016 149(3-4), 462-476. doi:10.1016/j.agrformet.2008.09.016

1017 Thom, A. S. (1972). Momentum, mass and heat exchange of vegetation. Quarterly Journal of the
1018 Royal Meteorological Society, 98(415), 124–134. doi:10.1002/qj.49709841510

1019 Tomasella, J., Silva Pinto Vieira, R. M., Barbosa, A. A., Rodriguez, D. A., Oliveira Santana, M. de, &
1020 Sestini, M. F. (2018). Desertification trends in the Northeast of Brazil over the period 2000–2016.
1021 International Journal of Applied Earth Observation and Geoinformation, 73, 197–206.
1022 doi:10.1016/j.jag.2018.06.012

1023 Trezza, R. (2006). Evapotranspiration from a remote sensing model for water mngement in an
1024 irrigation system in Venezuela. Interciencia, 31(6), 417-423

1025 Trezza, R., Allen, R., & Tasumi, M. (2013). Estimation of Actual Evapotranspiration along the Middle
1026 Rio Grande of New Mexico Using MODIS and Landsat Imagery with the METRIC Model. Remote
1027 Sensing, 5(10), 5397–5423. doi:10.3390/rs5105397

1028 Troufleau, D., Lhomme, J. P., Monteny, B., & Vidal, A. (1997). Sensible heat flux and radiometric
1029 surface temperature over sparse Sahelian vegetation. I. An experimental analysis of the kB- 1
1030 parameter. *Journal of Hydrology*, 188, 815-838. doi:10.1016/s0022-1694(96)03172-1

1031 Verhoef, A., De Bruin, H. A. R., & Van Den Hurk, B. J. J. M. (1997a). Some practical notes on the
1032 parameter kB- 1 for sparse vegetation. *Journal of Applied Meteorology*, 36(5), 560-572.
1033 doi:10.1175/1520-0450(1997)036%3C0560:spnotp%3E2.0.co;2

1034 Verhoef, A., McNaughton, K. G., & Jacobs, A. F. G. (1997b). A parameterization of momentum
1035 roughness length and displacement height for a wide range of canopy densities. *Hydrology and Earth
1036 System Sciences*, 1(1), 81–91. doi:10.5194/hess-1-81-1997

1037 Wang, C., Yang, J., Myint, S. W., Wang, Z.-H., & Tong, B. (2016). Empirical modeling and spatio-
1038 temporal patterns of urban evapotranspiration for the Phoenix metropolitan area, Arizona. *GIScience
1039 & Remote Sensing*, 53(6), 778–792. doi:10.1080/15481603.2016.1243399

1040 Wilson, K., Goldstein, A., Falge, E., Aubinet, M., Baldocchi, D., Berbigier, P., ... Verma, S. (2002).
1041 Energy balance closure at FLUXNET sites. *Agricultural and Forest Meteorology*, 113(1-4), 223–243.
1042 doi:10.1016/s0168-1923(02)00109-0

1043 WRB, I.W.G., 2006. World reference base for soil resources 2006, 2nd ed. In: FAO (ed.), *World Soil
1044 Resources Reports No. 103*, Rome. ISBN 92-5-105511-4.

1045 Wu, Q. (2020). geemap: A Python package for interactive mapping with Google Earth Engine.
1046 *Journal of Open Source Software*, 5(51), 2305. doi:10.21105/joss.02305

1047 Yin, L., Wang, X., Feng, X., Fu, B., & Chen, Y. (2020). A comparison of SSEBop-Model-Based
1048 evapotranspiration with eight evapotranspiration products in the Yellow River Basin, China. *Remote
1049 Sensing*, 12(16), 2528. doi:10.3390/rs12162528

1050 Zhang, Y., Kong, D., Gan, R., Chiew, F. H. S., McVicar, T. R., Zhang, Q., & Yang, Y. (2019). Coupled
1051 estimation of 500 m and 8-day resolution global evapotranspiration and gross primary production in
1052 2002–2017. *Remote Sensing of Environment*, 222, 165–182. doi:10.1016/j.rse.2018.12.031

1053 Zhao, M., Heinsch, F. A., Nemani, R. R., & Running, S. W. (2005). Improvements of the MODIS
 1054 terrestrial gross and net primary production global data set. *Remote sensing of Environment*, 95(2),
 1055 164-176. doi:10.1016/j.rse.2004.12.011

1056 **Supplementary material**

1057 Table S1. Performance statistics of the values observed with the STEEP model at each proposed
 1058 refinement (*z0m*, *rah* and remaining λET in the endmembers pixels) and their two by two
 1059 combinations. The comparison is made using the general basis of SEB models by RS as a reference,
 1060 that in our study was SEBAL.

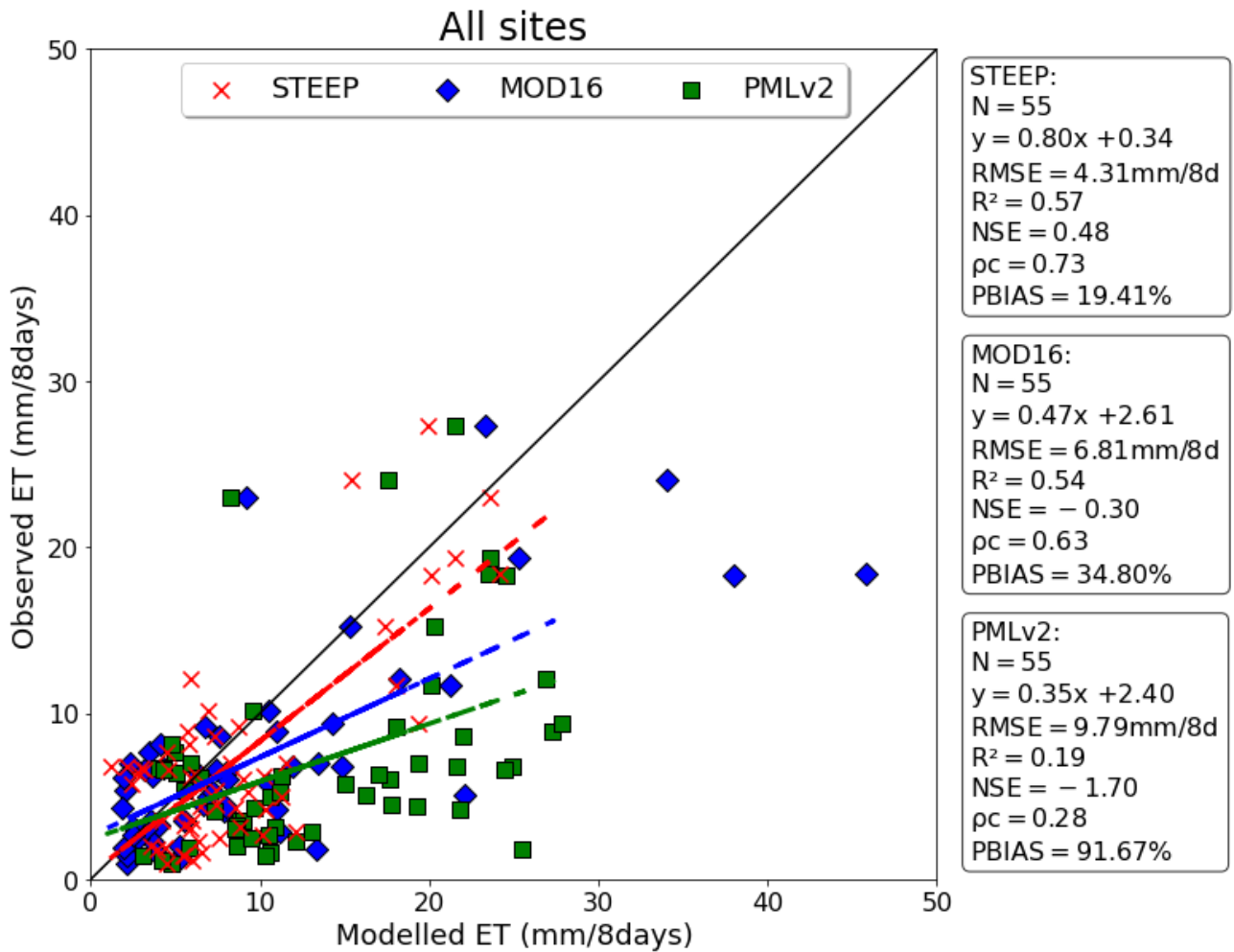
Site	Round	Performance statistics				
		<i>RMSE</i>	<i>R</i> ²	<i>NSE</i>	ρ_c	<i>PBIAS</i>
PTN (N = 252; 2011)	SEBAL	1.52	0.19	-0.45	0.34	47.30
	<i>z0m</i>	1.58	0.24	-0.37	0.39	36.54
	<i>rah</i>	1.41	0.21	-0.09	0.40	30.18
	<i>rλET</i>	0.95	0.55	0.51	0.67	-13.54
	<i>z0m</i> & <i>rah</i>	1.53	0.28	-0.28	0.42	31.25
	<i>z0m</i> & <i>rλET</i>	0.89	0.58	0.52	0.73	-15.79
	<i>rah</i> & <i>rλET</i>	1.01	0.41	0.39	0.61	-4.69
	STEPP	0.80	0.66	0.58	0.79	-17.27
SNN (N = 304; 2014)	SEBAL	1.08	0.55	0.39	0.67	40.62
	<i>z0m</i>	1.10	0.60	0.44	0.72	25.69
	<i>rah</i>	1.05	0.53	0.49	0.69	19.81
	<i>rλET</i>	0.99	0.64	0.55	0.65	-11.11

	<i>z0m & rah</i>	1.11	0.64	0.43	0.71	23.24
	<i>z0m & rλET</i>	0.79	0.64	0.63	0.75	5.32
	<i>rah & rλET</i>	0.92	0.55	0.51	0.64	14.23
	STEEP	0.76	0.69	0.65	0.80	20.80
	SEBAL	1.51	0.14	-3.69	0.18	143.58
	<i>z0m</i>	1.63	0.16	-4.48	0.19	112.36
	<i>rah</i>	1.37	0.12	-2.85	0.20	118.21
	<i>rλET</i>	0.72	0.20	0.01	0.37	33.07
SET (N = 283; 2015)	<i>z0m & rah</i>	1.69	0.22	-4.5	0.25	89.55
	<i>z0m & rλET</i>	0.78	0.09	-0.33	0.28	30.03
	<i>rah & rλET</i>	0.89	0.14	-0.57	0.29	59.55
	STEEP	0.85	0.24	-0.42	0.41	53.92
	SEBAL	1.64	0	-4.34	-0.03	84.79
	<i>z0m</i>	1.71	0.01	-4.32	-0.02	72.95
	<i>rah</i>	1.37	0	-2.40	-0.01	46.48
CGR (N = 201; 2014)	<i>rλET</i>	0.77	0.22	-0.19	0.45	16.21
	<i>z0m & rah</i>	1.66	0	-4	-0.01	62.45
	<i>z0m & rλET</i>	1.05	0.39	-0.85	0.48	43.26
	<i>rah & rλET</i>	0.94	0.28	-0.51	0.45	31.89

	STEEP	0.77	0.43	-0.17	0.61	11.89
	SEBAL	1.75	0.04	-1.48	-0.10	79.77
	<i>z0m</i>	1.97	0.06	-2.16	0.35	48.62
	<i>rah</i>	1.50	0.01	-0.83	0.05	57.22
CGR (N = 48; 2020)	<i>rλET</i>	0.99	0.25	0.20	0.37	19.19
	<i>z0m & rah</i>	1.89	0	-1.91	0.04	59.64
	<i>z0m & rλET</i>	1.13	0.19	-0.17	0.36	46.37
	<i>rah & rλET</i>	0.93	0.42	0.30	0.55	29.24
	STEEP	0.93	0.47	0.31	0.62	30.95

1061 *z0m* = roughness length for momentum transfer; *rah* = aerodynamic resistance for heat transfer;

1062 *rλET* = remaining *λET* in the endmembers pixels.



1063

1064 Figure S1. Evaluation of evapotranspiration (ET, mm/8days) observed and modelled with STEEP
 1065 (red crosses), MOD16 (blue diamonds) and PMLv2 (green squares) for all experimental sites
 1066 considering only where the field-observed data had eight consecutive days. The black line is the
 1067 1:1 line; dashed lines are the fitted linear regressions of observed on modelled values by the
 1068 STEEP model (red), MOD16 (blue) and PMLv2 (green) products.

1069 **Appendix A – Equations adopted to formulate the STEEP model**

1070 Latent heat flux was modeled using Eq. (A.1):

$$\lambda ET = R_n - G - H \tag{A.1}$$

1071 where λET is latent heat flux, R_n is net radiation, G is soil heat flux, and H is sensible heat flux. All
 1072 variables are expressed in energy units (e.g., W/m²).

1073 Net radiation was modeled based on the radiation budget indicated by Allen et al. (2007) and Ferreira
 1074 et al. (2020) by Eq. (A.2):

$$Rn = R_{S\downarrow} \times (1 - \alpha) + \varepsilon_S \times R_{L\downarrow} - R_{L\uparrow} \quad (A.2)$$

1075 where $R_{S\downarrow}$ is incident shortwave radiation (W/m^2), α is surface albedo (dimensionless), estimated
 1076 following Trezza et al. (2013), ε_S is surface emissivity (dimensionless), estimated following Long et
 1077 al. (2010), $R_{L\downarrow}$ is longwave radiation from the atmosphere (W/m^2); $R_{L\uparrow}$ is emitted longwave radiation
 1078 (W/m^2).

1079 Soil heat flux, expressed as a ratio of net radiation, was estimated following the model by
 1080 Bastiaanssen et al. (1998):

$$\frac{G}{Rn} = [(LST - 273.15) \times (0.0038 + 0.0074 \times \alpha) \times (1 - 0.98 \times NDVI^4)] \quad (A.3)$$

1081 where LST is the surface temperature (K) and NDVI is the Normalized Difference Vegetation Index
 1082 (dimensionless), estimated following Rouse et al. (1973).

1083 Sensible heat flux was modeled using:

$$H = \frac{\rho \times c_p \times dT}{rah} \quad (A.4)$$

1084 where ρ is the air density (kg/m^3), c_p refers to the specific heat of air at constant pressure ($J/kg/K$),
 1085 dT is the temperature gradient (K), and rah is the aerodynamic resistance for heat transfer (s/m).

1086

1087 Aerodynamic resistance to heat transport was estimated based on the classical equation given in
 1088 Paul et al. (2013), see also Verhoef et al. (1997a):

$$rah = \frac{1}{k \times u^*} \times \left[\ln \left(\frac{z_{ref} - d0}{z0m} \right) - \psi_h \right] + \frac{1}{k \times u^*} \times kB_{umd}^{-1} \quad (A.5)$$

1089 where k is the von Kármán constant taken as 0.41, u^* is the friction velocity (m/s), z_{ref} is the
 1090 reference height (m), $d0$ is zero plane displacement height (m), $z0m$ is roughness length for
 1091 momentum transfer (m), ψ_h is the atmospheric stability correction function for heat transfer (m), as
 1092 calculated following Paulson (1970), kB_{umd}^{-1} is the dimensionless parameter formulated to express
 1093 the excess resistance of heat transfer compared to momentum transfer, corrected for soil moisture
 1094 derived from remote sensing.

1095 The friction velocity was computed according to Verhoef et al. (1997b) and Paul et al. (2013):

$$u^* = k \times u \left[\ln \left(\frac{z_{ref} - d0}{z0m} \right) - \psi_m \right]^{-1} \quad (A.6)$$

1096 where u is the wind speed (m/s) at a known height z_{ref} , ψ_m is the atmospheric stability correction
 1097 function for momentum transfer (m), as calculated following Paulson (1970).

1098 Roughness length for momentum transport was estimated, based on the studies by Verhoef et al.
 1099 (1997b) and Paul et al. (2013):

$$z0m = (HGHT - d0) \times \exp^{(-k \times GAM + PSICORR)} \quad (A.7)$$

1100 where $HGHT$ is the height of the vegetation (m) and $PSICORR$ is taken as 0.2.

1101 Zero plane displacement height was obtained from:

$$d0 = HGHT \times \left[\left(1 - \frac{1}{\sqrt{CD1 \times PAI}} \right) + \left(\frac{\exp^{-\sqrt{CD1 \times PAI}}}{\sqrt{CD1 \times PAI}} \right) \right] \quad (A.8)$$

1102 where $CD1$ is taken as 20.6 and PAI is the Plant Area Index.

1103 GAM was obtained using:

$$GAM = \left(CD + CR \times \frac{PAI}{2} \right)^{-0.5} \quad (A.9)$$

1104 if $GAM < 3.33$, GAM is set to 3.33

1105 Plant Area Index was calculated according to Miranda et al. (2020) as:

$$PAI = 10.1 \times (\rho_{NIR} - \sqrt{\rho_{RED}}) + 3.1 \quad (A.10)$$

1106 where ρ_{NIR} is the near infrared band reflectance, and ρ_{RED} is the red band reflectance. If $PAI < 0$, $d0$
 1107 is set to 0.

1108 The dimensionless parameter kB_{umd}^{-1} is corrected by soil moisture by remote sensing following the
 1109 equations provided by Gokmen et al. (2012):

$$kB_{umd}^{-1} = SF \times kB^{-1} \quad (A.11)$$

1110 where SF is a scaling factor, represented by a sigmoid function:

$$SF = \left[c + \frac{1}{1 + \exp^{(d - e \times SM_{rel})}} \right] \quad (A.12)$$

1111 Here, c , d , e are the sigmoid function coefficients, for which we adopted values of 0.3, 2.5, and 4,
 1112 respectively, following Gokmen et al. (2012). SM_{rel} is the relative soil moisture, obtained from:

$$SM_{rel} = \frac{SM - SM_{min}}{SM_{max} - SM_{min}} \quad (A.13)$$

1113 where SM is the actual soil moisture content, in our case obtained with the GLDAS reanalysis
 1114 product, and SM_{min} and SM_{max} are the minimum and maximum soil moisture. The SM_{min} and SM_{max}
 1115 values were obtained using the annual time series analysis of the soil moisture data.

1116 kB^{-1} was calculated according to Su et al. (2001):

$$kB^{-1} = \frac{k \times Cd}{4 \times Ct \times \frac{u^*}{u(h)} \times \left(1 - \exp\left(-\frac{nec}{2}\right)\right)} \times f_c^2 + \frac{k \times \frac{u^*}{u(h)} \times \frac{z0m}{h}}{C_t^*} \times f_c^2 \times f_s^2 + kB_s^{-1} \times f_s^2 \quad (A.14)$$

1117 where $kB_s^{-1} = 2.46(Re^*)^{0.25} - 2$, Cd is the drag coefficient of the foliage elements taken as 0.2, Ct
 1118 is the heat transfer coefficient of the leaf with value 0.01.

1119 The ratio $\frac{u^*}{u(h)}$ is parameterized as:

$$\frac{u^*}{u(h)} = c1 - c2 \times \exp(-c3 \times Cd \times PAI) \quad (A.15)$$

1120 where $c1 = 0.320$, $c2 = 0.264$, $c3 = 15.1$.

1121 nec is the extinction coefficient of the wind speed profile within the canopy given by:

$$nec = \frac{Cd \times PAI}{\frac{2u^{*2}}{u(h)^2}} \quad (A.16)$$

1122 C_t^* is heat transfer coefficient of the soil given by:

$$C_{td}^* = Pr^{-2/3} \times (Re)^{-1/2} \quad (A.17)$$

1123 where Pr is the Prandtl number with a value 0.71, and Re is the Reynolds number calculated as:

$$Re = \frac{u^* \times 0.009}{\nu}, \quad \nu = 1.461 \times 10^{-5} \quad (A.18)$$

1124 where ν is the kinematic viscosity (m^2/s).

1125 In Eq. A.14 f_c is the fractional canopy cover calculated according to Eq. (A19), and f_s is its
 1126 complement.

$$f_c = 1 - \left[\frac{NDVI - NDVI_{min}}{NDVI_{max} - NDVI_{min}} \right]^{0.4631} \quad (A.19)$$

1127 where $NDVI_{max}$ and $NDVI_{min}$ are maximum and minimum NDVI values, respectively.

1128 dT in Eq. (A4) was estimated with a linear relationship on the surface temperature (Bastiaanssen et
1129 al., 1998) as:

$$dT = a + b \times LST \quad (A.20)$$

1130 To find the coefficients a and b in Eq. (A20) requires that hot and cold endmembers pixels are
1131 established. The coefficients were found as:

$$b = \frac{(dT_{hot} - dT_{cold})}{(LST_{hot} - LST_{cold})} \quad (A.21)$$

$$a = dT_{cold} - b \times LST_{cold} \quad (A.22)$$

$$dT_{hot/cold} = \frac{H_{hot/cold} \times rah_{hot/cold}}{\rho \times c_p} \quad (A.23)$$

$$H_{hot/cold} = Rn_{hot/cold} - G_{hot/cold} - \lambda ET_{hot/cold} \quad (A.24)$$

1132 where $dT_{hot/cold}$ are dT values for the hot/dry and cold/wet endmember pixels, respectively,

1133 $Rn_{hot/cold}$, $G_{hot/cold}$, $LST_{hot/cold}$, $rah_{hot/cold}$ are the median values extracted on the endmember
1134 pixels of each variable. The selection of endmember pixels is detailed in section 2.3.

1135 $\lambda ET_{hot/cold}$ is the term incorporated in the computation of H in the endmember pixels given by the
1136 Priestley-Taylor (1972) equation, according to Singh and Irmak (2011) and French et al. (2015):

$$\lambda ET_{hot/cold} = (Rn_{hot/cold} - G_{hot/cold}) \times f_c \times \alpha_{pt} \times \left[\frac{\Delta}{\Delta + \gamma} \right] \quad (A.25)$$

1137 where α_{pt} is the empirical Priestley-Taylor coefficient, nominally set to 1.26, but here adjusted
1138 according to local conditions, i.e. set to 0.55 and 1.75 for the hot and cold pixel in the endmembers,
1139 respectively. Δ is the slope of the saturation vapor pressure-air temperature curve (kPa/°C) and γ is
1140 the psychrometric constant (kPa/°C).

1141 The actual daily evapotranspiration (mm/day) was obtained by means of the following relationship:

$$ET_{24h} = \frac{86400}{(2.501 - 0.00236 \times T_a) \times 10^6} \times \frac{\lambda ET}{Rn - G} \times Rn_{24h} \quad (A.26)$$

1142 where T_a is the air temperature (°C), λET is derived from Eq. A1, and Rn_{24h} corresponds to the daily
1143 net radiation (W/m^2); in this study both driving variables were obtained with data from the ERA5-
1144 Land product.

1145